bioRxiv preprint doi: https://doi.org/10.1101/2021.07.15.452437; this version posted July 15, 2021. The copyright holder for this preprint (which was not certified by peer review) is the author/funder. All rights reserved. No reuse allowed without permission.

Decellularized Normal and Tumor Scaffolds for Cancer Organoid Cultures as a Model of Colorectal Peritoneal Metastases

Luca Varinelli[1,*], Marcello Guaglio[2,*], Silvia Brich[3,*], Susanna Zanutto[1], Antonino Belfiore[3], Federica Zanardi[4], Fabio Iannelli[4], Amanda Oldani[5], Elisa Costa[5], Matteo Chighizola[6], Simone P. Minardi[7], Stefano Fortuzzi[7], Martina Filugelli[8], Giovanna Garzone[8], Manuela Vecchi[7], Giancarlo Pruneri[3], Kusamura Shigeki[2], Dario Baratti[2], Laura Cattaneo[8], Dario Parazzoli[5], Alessandro Podestà[6], Massimo Milione[8], Marcello Deraco[2], Marco A. Pierotti[7] and Manuela Gariboldi[1,*]

[1] Department of Research, Fondazione IRCCS Istituto Nazionale Tumori, via G. Venezian 1, 20133 Milan, Italy.

[2] Peritoneal Surface Malignancies Unit, Colon and Rectal Surgery, Fondazione IRCCS Istituto Nazionale Tumori, via G. Venezian 1, 20133, Milan, Italy.

[3] Department of Pathology and Laboratory Medicine, Clinical Research lABoratory (CRAB), Fondazione IRCCS Istituto Nazionale Tumori, via G. Venezian 1, 20133, Milan, Italy.

[4] Bioinformatics Core Unit, IFOM, FIRC Institute of Molecular Oncology, via Adamello 16, 20139 Milan, Italy.

[5] Imaging Technological Development Unit, The FIRC Institute of Molecular Oncology, via Adamello 16, 20139, Milan, Italy.

[6] C.I.Ma.I.Na. and Dipartimento di Fisica "Aldo Pontremoli", Università degli Studi di Milano, via G. Celoria 16, 20133, Milan, Italy.

[7] Cogentech Ltd. Benefit Corporation with a Sole Shareholder, via Adamello 16, 20139 Milan, Italy.

bioRxiv preprint doi: https://doi.org/10.1101/2021.07.15.452437; this version posted July 15, 2021. The copyright holder for this preprint (which was not certified by peer review) is the author/funder. All rights reserved. No reuse allowed without permission.

[8] Pathology and Laboratory Medicine Department, Fondazione IRCCS Istituto Nazionale dei Tumori di Milano, via G. Venezian 1, 20133, Milan, Italy.

[*] These authors contributed equally: Luca Varinelli, Marcello Guaglio, Silvia Brich

Corresponding author: Manuela Gariboldi: manuela.gariboldi@istitutotumori.mi.it

Short title: Engineered 3D-models of the peritoneal metastatic niche

Abstract

Peritoneal metastases (PM) from colorectal cancer (CRC) are associated with poor survival. The extracellular matrix (ECM) plays a fundamental role in modulating the homing of CRC metastases to the peritoneum. The mechanisms underlying the interactions between metastatic cells and the ECM, however, remain poorly understood and the number of *in vitro* models available for the study of the peritoneal metastatic process is limited. Here, we show that decellularized ECM of the peritoneal cavity allows the growth of organoids obtained from PM, favoring the development of three-dimensional nodules that maintain the characteristics of *in vivo* PM. Organoids preferentially grow on scaffolds obtained from neoplastic peritoneum, which are characterized by greater stiffness than normal scaffolds. A gene expression analysis of organoids, grown on different substrates reflected faithfully the clinical and biological characteristics of the organoids. An impact of the ECM on the response to standard chemotherapy treatment for PM was also observed.

Significance: Evidence of the value of ex vivo 3D models obtained by combining patient-derived extracellular matrices depleted of cellular components and organoids to mimic the metastatic niche, to be used as a tool to develop new therapeutic strategies in a biologically relevant context, to personalize treatments and increase their efficacy.

bioRxiv preprint doi: https://doi.org/10.1101/2021.07.15.452437; this version posted July 15, 2021. The copyright holder for this preprint (which was not certified by peer review) is the author/funder. All rights reserved. No reuse allowed without permission.

Keywords: Colorectal cancer, Peritoneal metastasis, Organoids, Extracellular matrix (ECM), Decellularized extracellular matrix, engineered disease model, ECM stiffness.

Introduction

The peritoneum is the second most common site of metastasis for colorectal cancer (CRC) after the liver [1]. In the past, peritoneal metastases (PM) were considered a terminal condition, amenable only to palliative treatments. The advent of cytoreductive surgery and hyperthermic intraperitoneal chemotherapy (HIPEC) in the 1990s have allowed some patients with PM to achieve longterm survival, pushing the median overall survival from 16 to 51 months [2]. However, about 70% of treated patients still experience peritoneal relapse [3]. The development of preclinical cellular models that faithfully recapitulate PM pathology, therefore, is crucial for the identification of more effective therapeutic strategies.

The peritoneal metastatic cascade consists of a series of steps that begin with cell detachment from the primary tumor [4]. Fine-tuned interactions between biochemical factors and biomechanical events, such as remodeling of the extracellular matrix (ECM), govern the cascade and allow the formation of the metastatic niche [5, 6, 7, 8] . The metastatic niche facilitates organotrophic metastasis through the direct promotion of cancer stem cell survival, exploiting a tissue-specific microenvironment that is more suitable for the attachment of exfoliated neoplastic cells [5]. The biology behind these processes, however, is poorly understood due to the lack of organ-specific experimental models.

Most of the current data on metastatic spread have been obtained using cancer cell lines or patient-derived xenograft models, which do not fully reflect the physiopathology of their tumor of origin [9]. Tumor-derived organoids (TDOs) are an intermediate model between cell lines and xenografts; they grow three-dimensionally and retain cell–cell and cell–matrix interactions, which more closely reflect the characteristics of the original tumor. Importantly, organoids can be established in a short

bioRxiv preprint doi: https://doi.org/10.1101/2021.07.15.452437; this version posted July 15, 2021. The copyright holder for this preprint (which was not certified by peer review) is the author/funder. All rights reserved. No reuse allowed without permission.

time and are easy to manipulate [10]; they retain the genetic status of the original tissues and can be used to identify new therapeutic targets [11].

The possibility to isolate natural decellularized ECM and at the same time preserve both the 3D tissue architecture and the biochemical properties, enabling the development of more physiological cancer models [12, 13], prompted us to develop a tissue-engineered PM model for *in vitro* studies. Our model is based on the seeding of PM-derived organoids onto decellularized peritoneum-derived ECMs. Thanks to the possibility of characterizing the biochemical and biophysical properties of both organoids and ECM, the developed PM model allowed us to study the complex interactions between the ECM and neoplastic cells, by which we gained new insights into PM biology and the mechanisms underlying the cell-microenvironment interaction in this system.

Materials and Methods

Human tissues

Peritoneal tissue was collected from six patients with peritoneal metastatic colorectal carcinoma, who underwent surgical resection at the Peritoneal Malignancies Unit of our Institution. The patients were staged according to the WHO classification [14]. The study was approved by the Institutional review board (134/13; I249/19) and was conducted in accordance with the Declaration of Helsinki, 2009. Written informed consent was acquired. Metastatic lesions and apparently normal tissue (> 10 cm from the metastatic lesions) were harvested and one part of the metastatic tissue (1 cm in diameter) was placed in ice-cold PBS (ThermoFisher Scientific, Waltham, MA) containing gentamicin (50 ng/ml, ThermoFisher Scientific) and amphotericin B (50 ng/ml, ThermoFisher Scientific) for the generation of PM-derived organoids, while a second specimen was frozen in liquid nitrogen for molecular and histopathological analyses. The remaining tissue was used to develop 3D-decellularized matrices (3D-dECMs).

Normal tissue was partly used to develop 3D-decellularized matrices and partly frozen for further studies. FFPE blocks were prepared for IHC analyses of normal and metastatic tissue.

bioRxiv preprint doi: https://doi.org/10.1101/2021.07.15.452437; this version posted July 15, 2021. The copyright holder for this preprint (which was not certified by peer review) is the author/funder. All rights reserved. No reuse allowed without permission.

Development of PM-derived organoids

Tumor-derived tissue was cut into small pieces, washed with ice-cold PBS at least ten times, and subsequently digested with 500 U/ml collagenase type II (Sigma Aldrich, St.Louis, Missouri, USA) in DMEM-F12 for 1 hour at 37 °C with vigorous pipetting every 15 minutes. The remaining fragments were digested with 1 mg/ml trypsin, 5 mM EDTA (ThermoFisher Scientific) at 37 °C for 20 minutes. The supernatant was collected and centrifuged at 300 g for 5 minutes at 4 °C. The cell pellet was resuspended with Matrigel, growth factor reduced (Corning, NY, USA), and dispensed into 24-well cell culture plates (50 µl/well). After Matrigel polymerization, the cells were overlaid with 500 µl of basal cell culture medium consisting of Advanced DMEM-F12 (ThermoFisher Scientific) and supplemented with different growth factors (Supplementary Table S1) to mimic different niche factor conditions, as in Fujii *et al* [10]. Incubation was performed at 20% O_2 and 5% CO_2. After expansion, the TDOs were cultured in cell culture medium lacking growth factors, which was refreshed every three days. Optimal cell culture medium conditions were determined separately for each organoid culture (Supplementary Table S2).

Organoids were split every 1-2 weeks as follows: they were mechanically removed from the Matrigel by pipetting, incubated in Cell Recovery Solution (Corning) for 1 hour at 4 °C, washed twice with ice-cold PBS and seeded as described above.

Aliquots of each organoid culture were frozen or prepared for IHC analyses as follows: samples were fixed in 10% formalin at room temperature (RT) for 10 minutes and embedded into 200 µl Bio-Agar (Bio-Optica, Milan, Italy). The samples were then cooled at -20 °C until solidification. For each sample, sections of 3 µm were obtained.

Preparation of 3D-dECMs

3D-dECMs were derived from both PM and the corresponding normal peritoneum. Each experiment was conducted using three to ten different surgical specimens deriving from different patients.

bioRxiv preprint doi: https://doi.org/10.1101/2021.07.15.452437; this version posted July 15, 2021. The copyright holder for this preprint (which was not certified by peer review) is the author/funder. All rights reserved. No reuse allowed without permission.

The decellularization was performed as shown in Fig. 1B, according to the protocol described by Genovese et al. [13]. Briefly, both PM and normal peritoneum samples (60-100 mg wet weight) were kept in ice-cold PBS for 1 hour before processing. The specimens were split into two fragments, one of which was kept untreated for later comparison of the characteristics of the 3D-dECMs. For decellularization, the fragments were washed with ice-cold PBS supplemented with 50 ng/ml gentamicin and 50 ng/ml amphotericin B, followed by treatment with solutions containing detergents and enzymatic agents.

The success of the decellularization procedure was evaluated by analyzing the DNA content of the 3D-dECMs (see below). The 3D-dECMs were then washed with ice-cold PBS and either transferred into chilled freezing solution (90% DMEM-F12, 10% DMSO) and frozen for storage or fixed for IHC and immunofluorescence (IF) analyses. All the decellularization experiments were performed in triplicate, using at least three different samples, each derived from a different donor.

ex vivo engineered PM lesion

Engineered PM lesions were obtained from three organoid cultures (C1, C2 and C3). TDOs were removed from the Matrigel as described above and dissociated into single-cell suspensions with Trypsin-EDTA by vigorous pipetting for 10 minutes. About one million dissociated cells were counted with an automatic cell counter (ThermoFisher Scientific). 3D-dECMs derived from normal peritoneal tissue and PM were incubated overnight at 37 °C in DMEM-F12 supplemented with 10% FBS (Euroclone, Milan, Italy) and 50 ng/ml gentamicin and amphotericin B. To reduce intra-sample variability, the 3D-dECMs were cut into fragments of comparable sizes.

TDOs were resuspended in 1 ml cell culture medium (Supplementary Table S1) and seeded on the top of 50 mg of 3D-dECMs. Repopulated matrices were placed in a 24-well cell culture plate (Corning) containing DMEM-F12 supplemented with 10% FBS and 50 ng/ml gentamicin and amphotericin B, followed by incubation for 2 hours at 37 °C. Each well was filled with 2 ml cell culture medium, which was changed every two days (Fig. 1C). Repopulated matrices were either

bioRxiv preprint doi: https://doi.org/10.1101/2021.07.15.452437; this version posted July 15, 2021. The copyright holder for this preprint (which was not certified by peer review) is the author/funder. All rights reserved. No reuse allowed without permission.

frozen for RNA extraction or fixed for IHC and IF analyses. Representative 3 µm FFPE sections were cut at different depths to verify the presence of TDOs in the inner part of the 3D-dECM scaffold. The repopulation experiments were performed in triplicate, using three different neoplastic and normal-derived matrices obtained from three different donors.

Nucleic acid extraction

DNA from FFPE sections of the PM-derived organoids and their tissue of origin was used for mutational analysis. DNA was extracted using the Masterpure Complete DNA Purification Kit (Lucigen-Biosearch Technologies, Middleton, WI, USA) and quantified on the QIAxpert® spectrophotometer (QIAGEN, Hilden, Germany).

DNA from 20 mg of normal peritoneum and PMs, both decellularized and untreated, was used to evaluate the success of the decellularization procedure. DNA was extracted using the DNeasy Blood&Tissue kit (QIAGEN) according to the manufacturer's instructions, and quantified using Nanodrop 1000 (ThermoFisher Scientific) at 260/280 nm ratio. DNA from decellularized ECM, normal peritoneum, PM, and their corresponding non-decellularized samples was loaded onto a 1% agarose gel. The separated bands were visualized by exposing the gel to UV light and images were acquired using Gel Doc (Bio-Rad, Hercules, CA, USA). All of the experiments were performed in triplicate. RNA from the three organoid cultures (C1, C2 and C3) grown both in Matrigel and on normal or neoplastic peritoneal 3D-dECMs was used for RNA-seq analyses. For the PM organoids, the Matrigel was digested with Cell Recovery Solution (Corning) as described above. The pellet was washed three times with ice-cold PBS and suspended in 1 ml TRIzol™ reagent (QIAGEN). Instead, for the repopulated 3D-dECMs, the matrices were washed three times with ice-cold PBS and homogenized using the TISSUE Tearor Homogenizer (QIAGEN) in 500 µl TRIzol™ reagent (QIAGEN). Then, RNA was extracted following the manufacturer's instructions, quantified on a ND-1000 spectrophotometer (ThermoFisher Scientific) and stored at -80 °C.

bioRxiv preprint doi: https://doi.org/10.1101/2021.07.15.452437; this version posted July 15, 2021. The copyright holder for this preprint (which was not certified by peer review) is the author/funder. All rights reserved. No reuse allowed without permission.

Histochemistry (HC), IHC and IF

Before HC and IHC staining, FFPE sections were cut into slices and dewaxed in xylene, rehydrated through decreasing concentrations of ethanol and washed with water. Slices were stained with H&E for quality control. For HC analysis, sections were stained with Masson's trichrome (Aniline blue kit; Bio-Optica), Alcian blue stain (pH 2.5 kit, Bio-Optica), van Gieson trichrome (Bio-Optica), and Periodic Acid Schiff (PAS, Bio-Optica) following the manufacturers' instructions. IHC was performed using the following mouse anti-human monoclonal antibodies: Ki-67, CK19, CK20, CK AE1/AE3, CDX2, LGR5, and vimentin. Images were acquired with a DM6000B microscope (Leica). Staining was performed automatically, using theAutostainer Link 48 (Dako, Agilent, Santa Clara, CA. US). Dilutions and experimental conditions are listed in Supplementary Table S3. For IF analyses, FFPE sections were stained with Alexa680-conjugated Wheat Germ Agglutinin (WGA) marker (ThermoFisher Scientific) and DAPI (VECTASHIELD Mounting Medium with DAPI, Maravai LifeScencies, San Diego, CA, USA), with anti-human Ki-67 and LGR5 monoclonal antibodies, with anti-human Collagen-IV and anti-human monoclonal cCASPASE3 antibodies and DAPI, followed by Alexa488-conjugate goat anti-mouse or Alexa546-conjugated goat anti-rabbit IgG polyclonal secondary antibodies for 1 hour at RT in dark (ThermoFisher Scientific). Images were acquired with a DM6000B microscope (Wetzlar, Germany Leica,) equipped with a 100 W mercury lamp, and analyzed using Cytovision software (Leica). Dilutions and experimental conditions are listed in Supplementary Table S3.

DNA sequencing

About 150–200 ng genomic DNA (measured with Qubit dsDNA HS assay kit, ThermoFisher Scientific), were sheared by the Sure Select Enzymatic Fragmentation kit (Agilent Technologies Inc., Santa Clara, CA, USA). NGS libraries were created using Sure Select XT2 Low input Custom library probes (Agilent Technologies Inc.). The probe set was custom designed by Cogentech (OncoPan panel) and includes the exonic regions of the following genes: APC, ATM, BARD1,

bioRxiv preprint doi: https://doi.org/10.1101/2021.07.15.452437; this version posted July 15, 2021. The copyright holder for this preprint (which was not certified by peer review) is the author/funder. All rights reserved. No reuse allowed without permission.

BMPR1A, BRCA1, BRCA2, BRIP1, CDH1, CDKN2A (α and β isoform), CDK4 (exon 2), CHEK2 , CTNNA1, EPCAM , FANCM, MLH1, MSH2, MSH3, MSH6, MUTYH, NBN, NHTL1, PALB2, PMS2, POLD1, POLE, PTEN, RAD51C, RAD51D, SMAD4, STK11, TP53, KRAS, NRAS, BRAF, EGFR, HER2 (ERBB2), and PIK3CA. Sequencing was performed on Illumina MiSeq platform, in PE mode (2 x 150 bp). Raw reads were demultiplexed and aligned to a reference genome (Human GRCh37) using a pipeline developed in-house in collaboration with enGenome Software Company and annotated with the eVai tool. Results were compared to find the percentage of common SNVs (Single Nucletode Variants). Five PM-derived organoids (C1, C2, C3, C4 and C6) and their corresponding surgical samples were analyzed. FFPE tissue for C5, unfortunately,was not available.

Morphological evaluation of the decellularized matrices

3D-dECMs from normal peritoneum and PM lesions were washed twice with 1X PBS and placed in a 60 mm petri dish. Samples were illuminated with a widefield lamp laser to visualize the architecture of the collagen fibers. An image format of 1024x1024 pixels was used and all images were acquired with Leica Application Suite X, ver. 3 software. 3D-dECMs FFPE sections deriving from normal and PM peritoneum were used to perform polarized light microscopy (PLM). FFPEs were analyzed with an Olympus BX63 upright widefield microscope equipped with a motorized stage and a Hamamatsu OrcaAG camera, using Metamorph software. UplanSApo 4X/0.16 N.A objective was used to acquire the mosaics of the sections. Insets were acquired with UplanSApo 10X/0.4 N.A. and UplanSApo 20X/0.75 N.A. objectives. All experiments were perfomed at least in duplicate. Confocal reflection microscopy images were acquired with a Leica TCS SP8 laser confocal scanner mounted on a Leica DMi8 microscope through a HC PL FLUOTAR 20×/0.5 NA.

Nanoscale topographical analysis of 3D-dECMs

bioRxiv preprint doi: https://doi.org/10.1101/2021.07.15.452437; this version posted July 15, 2021. The copyright holder for this preprint (which was not certified by peer review) is the author/funder. All rights reserved. No reuse allowed without permission.

The topographical evaluation of the 3D-dECMs was performed by AFM on samples deriving from normal peritoneum and PM of three different patients. Before the AFM analysis, the 3D-dECM slides were left for 30 minutes at RT to dissolve the optimal cutting temperature (OCT) compound. Then, the samples were carefully washed with ultrapure water and covered with 1X PBS buffer. AFM topographic measurements were carried out at RT using a NanoWizard3 AFM (JPK, Germany) coupled to an Olympus BX61 inverted microscope and equipped with tapping mode silicon ACTG AFM probes (APPNANO). The 50 µm thick tissue slices, instead, were mounted on polarized glass slides (ThermoFisher Scientific), left for 30 minutes at RT and carefully washed with ultrapure water. The topography of each tissue was characterized by collecting at least 10 areas (5x5 μm^2) of the sample surface with 512×512 points (scan speed 3,5 $\mu m\ s^{-1}$).

ECM component quantification

Total collagen and sulphated glycosaminoglycan (sGAG) content on fresh and decellularized peritoneum (both normal and PM) were quantified using the SIRCOL collagen assay (Biocolor, Carrickfergus, UK) and the Blyscan GAG assay kit (Biocolor), respectively. The experiments were performed in triplicate following the manufacturer's instruction. Data are the mean of three different neoplastic and normal-derived samples obtained from three different donors.

Nanoindentation measurements by AFM

AFM mechanical analysis was carried out on 3D-dECMs deriving from normal peritoneum and PM of three patients (see Fig. 2). 3D-dECMs were embedded in OCT and frozen with nitrogen-cooled 2-propanol for 10 seconds. Slices of 100 µm thickness were cut with a microtome (Leica) and attached to positively charged poly-lysine coated glass coverslips (ThermoFisher Scientific), exploiting the electrostatic interaction. Nanomechanical tests were performed in liquid on samples covered by a PBS droplet confined by a circular ridge of hydrophobic two-component silicone paste (Leica). A Bioscope Catalyst AFM (Bruker) was used, which was resting on an active anti-vibration

bioRxiv preprint doi: https://doi.org/10.1101/2021.07.15.452437; this version posted July 15, 2021. The copyright holder for this preprint (which was not certified by peer review) is the author/funder. All rights reserved. No reuse allowed without permission.

base (DVIA-T45, Daeil Systems) and put into an acoustic enclosure (Schaefer). The measurements were performed at RT.

Custom monolithic borosilicate glass probes consisting of spherical glass beads (SPI Supplies), with radii R in the range of 7.5–9.5 μm, were attached to tipless cantilevers (Nanosensor, TL-FM) with nominal spring constant k = 2.8 N/m. Probes were fabricated and calibrated, in terms of tip radius, according to an established custom protocol [15]. The spring constant was measured using the thermal noise calibration [16, 17] and corrected for the contribution of the added mass of the sphere [18, 19]. The deflection sensitivity was calibrated *in situ* and non-invasively before every experiment by using the previously characterized spring constant as a reference, according to the SNAP procedure described in [20].

The mechanical properties of the 3D-dECMs were obtained by fitting the Hertz model to sets of force versus indentation curves (simply force curves, FCs), as described elsewhere [20, 21, 22, 23], to exctract the value of the YM of elasticity, which measures ECM rigidity. FCs were collected in Point and Shoot (P&S) mode, selecting the regions of interest from optical images, exploiting the accurate alignment of the optical and AFM images obtained using the Miro software module integrated in the AFM software. Each set of FCs consisted of an array of 15x15=225 FCs spatially separated by approximately 10 μm, each FC containing 8192 points, with ramp length L = 8 μm, maximum load Fmax = 150 nN, and ramp frequency f = 1 Hz. Typical maximum indentation was 3-4 μm. Typical probe velocity during indentation was 16 μm/s.

Three samples were characterized for each condition. In each sample, three P&S, each made of 225 FCs, were recorded in macroscopically separated locations, resulting in ~2000 FCs per patient condition.

Stem cell maintenance, proliferation and apoptosis assays

Growing cells, stem cells and apoptotic cells were detected on FFPE sections. Growing cells, deriving from disaggregated TDOs, were stained with anti-human Ki-67 monoclonal antibody

bioRxiv preprint doi: https://doi.org/10.1101/2021.07.15.452437; this version posted July 15, 2021. The copyright holder for this preprint (which was not certified by peer review) is the author/funder. All rights reserved. No reuse allowed without permission.

(clone MIB-1) and DAPI, and their growth rate was expressed as the percentage of Ki-67-positive cells present in fields devoid of dead cells. Stem cells were stained with anti-human LGR5 monoclonal antibody (clone OTI2A2) and DAPI, and their density was expressed as the percentage of LGR5-positive cells present in fields devoid of dead cells. Apoptotic cells were stained with anti-human cCASPASE3 monoclonal antibody (clone 9661) and DAPI, and the apoptotic rate was calculated as the percentage of cCASPASE3-positive cells present in the field. The percentage of Ki-67-positive, LGR5-positive and cCASPASE3-positive cells was obtained by dividing the number of positive cell present in one field by the total number of cells in one field, multiplied by 100. Cells in three independent fields (40X magnification) were counted using ImageJ software. The experiments were performed in triplicate using three different neoplastic and normal-derived matrices obtained from three different donors.

RNA-seq analysis

Gene expression profiles were conducted on C1, C2 and C3 organoid cultures grown in Matrigel and on 3D-dECMs. Total RNA was extracted using TRIzol™ reagent (QIAGEN). Qubit fluorimeter (ThermoFisher Scientific) and Agilent Bioanalyzer 2100 (RIN > 8) were used to measure and assess RNA abundance and integrity, respectively. Indexed library preparation was performed starting with 500 ng total RNA with the TruSeq stranded mRNA (Illumina) according to the manufacturer's instructions. RNA-seq was performed in PE mode (2x75nt) on an Illumina NextSeq550 platform, generating an average of 55 million PE reads per sample. For every condition (Matrigel, normal 3D-dCM and neoplastic 3D-dECM), two replicates per organoid were sequenced, for a total of 18 data points. Raw reads were aligned to the human transcriptome (hg38) with STAR [24] using the quantMode option to generate transcripts counts. Differentially expressed genes in the three growth conditions were identified with DESeq2 [25]. All *p*-values were adjusted for false discovery rate with the Benjamini-Hochberg method.

bioRxiv preprint doi: https://doi.org/10.1101/2021.07.15.452437; this version posted July 15, 2021. The copyright holder for this preprint (which was not certified by peer review) is the author/funder. All rights reserved. No reuse allowed without permission.

Gene Set Enrichment Analysis

Gene Set Enrichment Analysis was performed with the enrichR R package [26] on deregulated genes (absolute fold change > 2 and adjusted *p*-value <0.05). In particular, the enrichment for the Matrisome database was assessed. This database provides live cross-referencing to gene and protein databases for every ECM and ECM-associated gene, also integrating experimental proteomic data on ECM and ECM-associated proteins and genes from the ECM Atlas [27]. Gene sets with adjusted *p*-value <0.05 were considered significantly enriched.

Treatment with cytotoxic drugs

For the *in vitro* simulation of HIPEC treatment, mitomycin-c (Kyowa Kirin Co., Ltd., Tokyo, Japan) was used at a concentration of 35 mg/m^2, which corresponds to 17.5 mg/l for *in vitro* treatments [28]. Mitomycin-c was dissolved in DMSO to obtain a 100 mg/l stock solution and diluted to the working concentration in the cell culture medium. The final solvent concentration was <0.1% for all samples, including controls. The experiments were performed in triplicate, using three different neoplastic and normal-derived matricies obtained from three different donors.

ex vivo PM lesion to test HIPEC efficacy *in vitro*

The *in vitro* surrogate model of PM disease mimicking HIPEC intervention was designed as reported by Ubink et al. [28]. An *ex vivo* engineered micrometastasis that reproduces the binding of CRC circulating metastatic cells to the peritoneum was obtained by growing PM-derived organoids on 3D-dECMs from neoplastic peritoneum. In the model, PM-derived organoids were in contact with the drug, as during HIPEC. Briefly, PM-derived organoids were grown on the top of neoplastic 3D-dECMs in a 24-well cell culture plate for 12 days in order to allow a complete colonization of the matrix [12, 13, 29]. TDOs grown in Matrigel were used as control to evaluate the impact of native 3D-dECMs on the HIPEC treatment. The engineered PM lesions were treated with preheated mitomycin-c at a concentration of 17.5 mg/l for 1 hour at 42.5 °C, which is in line with the current

bioRxiv preprint doi: https://doi.org/10.1101/2021.07.15.452437; this version posted July 15, 2021. The copyright holder for this preprint (which was not certified by peer review) is the author/funder. All rights reserved. No reuse allowed without permission.

standard protocol used for HIPEC at Fondazione IRCCS Istituto Nazionale dei Tumori - Milano Institution, whereafter the PM models were subjected to three washes with 1X PBS and incubated for 48 hours with appropriate cell growth medium (Fig. 1D).

Samples were fixed in formalin and FFPE sections were obtained as described above. The impact of HIPEC treatment on TDO proliferation and the activation of an apoptotic program were determined by Ki-67 and cCASPASE3 immunostaining, respectively. All experiments were performed in triplicate using three different neoplastic and normal-derived matricies obtained from three different donors.

Statistical analyses

Statistical analyses were performed using GraphPad Prism software (version 8.4.1 (676), GraphPad Software, San Diego, USA). Data are expressed as mean and SEM. A two-sided Student's *t*-test was used to compare paired groups. Differences among groups were evaluated using two-way ANOVA.

In the case of AFM mechanical experiments, for each patient and each condition tested, the median values of the YM were extracted from each measured location, and the associated effective errors were calculated by using the procedure described in Cramer et al [23, 30]. The distributions of the measured YM values were obtained by grouping all values measured in all locations, for each patient and each condition tested. The statistical significance of differences between results obtained for the two conditions was estimated by applying the two-tailed *t*-test. A p-value <0.05 was considered statistically significant.

Results

Development of PM-derived organoids

Six organoid cultures (C1 to C6) were developed from PM, following established protocols [10, 31], as detailed in the Materials and Methods section. The main characteristics of the patients from

bioRxiv preprint doi: https://doi.org/10.1101/2021.07.15.452437; this version posted July 15, 2021. The copyright holder for this preprint (which was not certified by peer review) is the author/funder. All rights reserved. No reuse allowed without permission.

which the organoids were derived are summarized in Supplementary Table S4. In line with previous works on organoids from advanced CRC [10, 31], the growth of the organoids required supplementation of minimal niche factors. Organoids carrying mutations in the *KRAS* gene required EGF or noggin-1 supplementation, while organoids carrying *FGR1* amplification grew in medium without EGF. The *BRAF*-mutant TDOs grew in a medium with minimal requirements for the niche factors. These results highlight how the different mutational profiles lead to specific requests of niche factors [10](Supplementary Table S1).

PM-derived organoid characterization

PM-derived organoids preserved the main characteristics of their tissues of origin, expressing the colorectal specific markers CK AE1/AE3, CK19, CK20, and CDX2 (Fig. 2A, Supplementary Fig. S1A and S1C).

The TDOs exhibited the typical glandular features observed in the corresponding surgical sample, including signet-ring cells, nest-like growth pattern, nuclear atypia, cuboidal nuclear morphology and pleomorphism, and had a similar degree of differentiation to that of the parental cancer (Fig. 2A and 2B).

All organoids and corresponding clinical samples were positive for the Leucine-rich repeat-containing G-protein coupled receptor 5 (LGR5), the well-established stem cell marker for the colonic niche [11] (Fig. 2C, Supplementary Fig. S1B and S1D). The organoids were also Ki-67-positive, suggesting that they underwent active proliferation (Fig. 2A, Supplementary Fig. S1A and S1C). Moreover, the TDO mutational profile was very similar to that of the tumor of origin (Fig. 2D, Supplementary Fig. S1E).

Development of 3D-dECMs

3D-dECMs from PM and normal peritoneum were generated following the protocol described by Genovese et al. [13]. DNA quantification showed almost total DNA depletion after the

bioRxiv preprint doi: https://doi.org/10.1101/2021.07.15.452437; this version posted July 15, 2021. The copyright holder for this preprint (which was not certified by peer review) is the author/funder. All rights reserved. No reuse allowed without permission.

decellularization procedure (***p<0.001; Fig. 3A Supplementary Fig.S2A). Fluorescence analysis of formalin-fixed, paraffin-embedded (FFPE) sections highlighted the complete removal of the nuclei and lipids form the cellular membranes (Fig. 3B). Immunohystochemistry (IHC) analysis showed loss of cytokeratins and vimentin, indicating the absence of epithelial and mesenchymal cells, respectively, and the maintenance of collagen IV distribution, the main structural protein (Fig. 3C).

Heamtoxilin and Eosin (H&E), van Gienson and Masson trichrome staining revealed the maintainance of the architectural structure of the corresponding non-decellularized samples (Fig. 3C and 3D).

Finally, lyophilyzed 3D-dECMs were added to the culture media but no differences were observed in cell viability after 72 hours of growth, indicating that the decellularization procedure has no cytotoxic effects (Supplementary Fig. S2B).

3D-dEMCs: morphological features and mechanical properties

Confocal reflection and polarized light microscopy techniques showed that the differences between normal and neoplastic-derived tissues obtained from three different PM patients were related both to the tissue texture and to the distribution and integrity of the single collagen fiber (Fig. 4A). The 3D-dECMs of normal tissues showed higher density and clusters of collagen fibers, with random relative orientation; in the neoplastic 3D-dECMs, the collagen structure seems more irregular and porous, although a tendency to fiber alignment and formation of bundles on the larger scale can be observed.

Atomic Force Microscopy (AFM) topographical analysis highlighted an asymmetric distribution of collagen at the micrometer scale: matrices derived from normal tissues are organized in groups of very thin, intersecting fibers (with diameters below 50nm), characterized by a variety of orientations, while matrices derived from neoplastic tissues had a more corrugated and disordered surface pattern (Fig. 4B). At odd with the case of ECM derived from healthy and CRC-affected

bioRxiv preprint doi: https://doi.org/10.1101/2021.07.15.452437; this version posted July 15, 2021. The copyright holder for this preprint (which was not certified by peer review) is the author/funder. All rights reserved. No reuse allowed without permission.

tissues [21], we do not observe a clear tendency of collagen fibers to form aligned bundles in the neoplastic state, although at this small scale the neoplastic matrix seems to be structurally more compact than the normal ECM. The increased anisotropy of the ECM structure reported in Nebuloni et al. [21] in the case of CRC is more evident in the optical confocal image of the neoplastic sample (Fig. 4A). Collagen was less abundant in neoplastic tissue compared with normal tissue, however, the latter showed higher levels of glycosaminoglycans GAGs. Both collagen and GAG levels decreased in decellularized samples (about 20% of loss in 3D-dECMs $^{**}p<0.01$; Fig. 4C).

The neoplastic 3D-dECMs showed a broader distribution of Young Modulus (YM) values and were markedly stiffer than the normal 3D-dECMs (Fig. 4D). Hovewer, the YM distributions are considerably scattered and a significant overlap is present between the two conditions. These results indicate that the ECM is a complex system that remains locally heterogeneous on the scale of several typical cellular lengths, i.e., 10-100 µm, because the transition from the normal to the neoplastic condition, in terms of change of stiffness and structural organization, is not uniform across the whole macroscopic tissue region.

Fig. 4E shows the median values of the YM measured in the different conditions: the stiffening is statistically significant for all three patients, which is confirmed by the results shown in Fig. 4E, normalized to the mean YM value of the healthy samples. Of note, the strongest relative stiffening in the tumor tissue, with an increase in the YM value of more than 300%, was measured in the tumor sample from the patient who had the normal softest 3D-dECM (Pt1) (Fig. 4F, Supplementary Fig. S3A).

Decellularized scaffolds sustain PM-derived organoid growth

To develop an *in vitro* model of PM disease, we repopulated 3D-dECMs with C1, C2 and C3 TDOs, with mutational profiles that resemble the most common gene alterations in CRC (C1 was KRAS-mutant,C2 BRAF-mutant, while C3 had FGFR1 amplified).

bioRxiv preprint doi: https://doi.org/10.1101/2021.07.15.452437; this version posted July 15, 2021. The copyright holder for this preprint (which was not certified by peer review) is the author/funder. All rights reserved. No reuse allowed without permission.

In line with data from literature, showing that colonization of decellularized matrices requires from eight to twelve days, we chose to let grow the organoids on the matrices for five, 12 and 21 days [12, 13, 29].

Five days after seeding, C1 organoids were localized along the perimeter of the 3D-dECMs generated from normal peritoneum (Fig. 5A). A similar distribution was observed 12 and 21 days after seeding, with a slight increase in the number of cells in the stromal region. In 3D-dECMs generated from neoplastic peritoneum, instead, C1 TDOs were distributed throughout the matrix five days after seeding, and colonization was evident with high stromal infiltration on day 21 (Fig. 5A and Supplementary Fig. S5A and S5B).

Morphological characteristics and the efficiency of TDO infiltration were correlated with grade and differentiation state of their tumours of origin. Organoids deriving from metastatic grade III/G2 lesions, with a moderate undifferentiation and low invasive ability (C1), infiltrated into the 3D-dECM as single cells, while organoids originating from grade IV/G3 poorly undifferentiated tumors with BRAF mutation (C2) and FGFR1 amplification (C3), infiltrated into the 3D-dECMs and maintained the spheroid shape (Fig.5A, Supplementary Fig. S4A and S4B).

3D decellularized scaffolds support the proliferation of organoids

Results showed that 3D-dECMs generated from neoplastic peritoneum had a significantly higher percentage of Ki-67-positive cells 5 and 12 days (***$p<0.001$) after seeding, indicating that these organoids underwent a faster growth (Fig. 5B, C and Supplementary Material S4C, S4E, S4F and S4G). No differences were observed 21 days after seeding. After 12 days of growth, the Ki-67-positive fraction was lower that in cells cultured for five days; however at both time points the Ki-67-positive fraction was greater in cells grown on neoplastic matrix than in those cultured on normal matrix, highlighting that the neoplastic 3D-dECMs promotes TDO proliferation.

LGR5-positive staining highlighted that the stem cell pool was maintained in both normal and neoplastic 3D-dECMs 5 and 12 days after seeding (Fig. 5D and 5E), At day 21 the stem cell pool

bioRxiv preprint doi: https://doi.org/10.1101/2021.07.15.452437; this version posted July 15, 2021. The copyright holder for this preprint (which was not certified by peer review) is the author/funder. All rights reserved. No reuse allowed without permission.

was significantly lower in 3D-dECMs generated from normal peritoneum compared with 3D-dECMs generated from neoplastic peritoneum. Most likely, after 21 days of growth, the cells are at confluence and the stem cells pool grown on the neoplastic matrix has an environment that favors maintainance of its phenotype.

ex vivo engineered PM lesions reproduce patient PM

IHC analysis of the TDOs using colorectal markers showed that repopulated 3D-dECMs retain the main characteristics and the morphology of their tumor of origin (Fig. 6A and Supplementary Fig. S5A and S5C), presenting the typical histological features observed in PM patients, such as: i) signet ring cells, ii) bizarre mitotic figures, iii) necrotic debris, iv) pleomorphic cell size and shape, and v) multinucleated cells (Fig. 6B and Supplementary Fig. S5B and S5D). Signet ring cells have been reported in another *ex vivo* model system [32], highlighting that our model of PM is highly representative of *in vivo* lesions.

Gene expression analysis of engineered PM lesions

RNA sequencing (RNA-seq) analysis of the TDOs (Fig. 7) highlighted differences between 3D-dECMs and Matrigel substrates: 327 differentially expressed genes (DEGs) were identified in TDOs grown on normal 3D-dECMs, and 144 DEGs were identified in TDOs grown on neoplastic 3D-dECMs compared to TDOs grown in Matrigel ($|FC| > 1.5$ and adj p-value <0.05).

The most represented biological processes include cell-cell/cell-matrix interactions, organoid behavior and interactions with the ECM, angiogenesis, metal ion homeostasis, and response to external stimuli. 3D-dECMs deregulated many genes fundamental for the 3D-architecture/organization of the ECM. Many of the up-regulated genes identified in TDOs grown on neoplastic 3D-dECM were assigned to the Matrisome database (67% for neoplastic versus normal 3D-dECM, and 25% for neoplastic 3D-dECM versus Matrigel). Only 8% of the up-regulated genes identified in TDOs grown on normal 3D-dECM versus TDOs grown in Matrigel belonged to the

bioRxiv preprint doi: https://doi.org/10.1101/2021.07.15.452437; this version posted July 15, 2021. The copyright holder for this preprint (which was not certified by peer review) is the author/funder. All rights reserved. No reuse allowed without permission.

Matrisome database (Fig. 7A). Unsupervised hierarchical clustering of TDOs highlighted a clear separation between TDOs grown on neoplastic 3D-dECM and TDOs grown on normal 3D-dECM and in Matrigel substrates (Fig. 7B and Supplementary Fig. S6A and S6B). TDOs grown on both normal and neoplastic 3D-dECMs presented an over-representation of DEGs involved in ECM composition, regulation and modulation (Fig. 7C). Growth on 3D-dECM also favors the expression of genes involved in the regulation of angiogenic processes, the response to cytokine stimuli, the integrin pathway, as well as copper and zinc metabolism. The same categories were found for both normal and neoplastic-derived 3D-dECMs (Supplementary Fig. S7C and S7D).

Using the Matrisome database, we identified genes related to the core composition of the ECM and to of ECM interactors/regulators through secretion of specific factors, all of which were higher in 3D-dECMs derived from neoplastic tissue (Fig. 7D and Supplementary Fig. S6E, S6F, S6G and S6H). 3D-dECMs presented high expression of genes involved in stem cell pathways, the cellular response to cytokines, zinc and copper metabolism, the integrin pathway, and the regulation of angiogenesis (Fig. 7E and Supplementary Fig. S6E, S6F, S6G and S6H). Similar results were found for genes involved in cell-cell/cell-matrix interactions (Fig. 7F).

3D-dECMs decrease the efficacy of HIPEC treatments

C1, C2 and C3 organoids were treated with a dose of Mitomycin-c at 17.5 mg/l scaled up from the dose administered to patients during HIPEC treatment at our Institution. TDOs were grown on the neoplastic-derrived 3D-dECMs for 12 days, which is considered sufficient for the colonization of the matrix's surface [29]. Mitomycin-c treatment of repopulated neoplastic 3D-dECMs and TDOs grown in Matrigel induced cellular disruption in C1 and C3 organoids (Supplementary Fig. S7A). Ki-67 expression decreased in the treated group, also showing a diffuse cytoplasmatic signal (Supplementary Fig. S7B). The number of Ki-67-positive C1 organoid cells grown in Matrigel or on 3D-dECMs was reduced by 95% and 72%, respectively, compared to the untreated control groups (**$p<0.01$; Fig. 8A and 8C). Proliferation was reduced by 80% and 66%, respectively, in C3

bioRxiv preprint doi: https://doi.org/10.1101/2021.07.15.452437; this version posted July 15, 2021. The copyright holder for this preprint (which was not certified by peer review) is the author/funder. All rights reserved. No reuse allowed without permission.

organoids grown in Matrigel or on 3D-dECM compared to the untreated control groups (**p<0.01; Fig. 8A and 8C). Immunofluorescence (IF) staining with clavated CASPASE3 (cCASPASE3) confirmed that untreated C1 and C3 TDOs were alive (Fig. 8B, left panel). Mitomycin-c treatment induced CASPASE3 cleavage, demonstrating that HIPEC simulation induces cell death through induction of apoptosis (Fig. 8B, right panel). Mitomycin-c treatment was not effective on C2 organoids (Supplementary Fig. S7C).

Discussion

Here, we describe an engineered model that combines key features of TDOs within the microenvironment, enabling the recapitulation of the PM niche under physiological conditions. Transcriptome analysis showed that organoids grown on peritoneal matrices express genes involved in pathways that favor implantation into the matrix and remodelling of the ECM. The 3D-dECM models reproduce the complex tissue architecture and cell-matrix interactions of the native environment of PM. 3D-dECMs derived from the neoplastic peritoneum allow the development of a tissue microenvironment that preserves the stem cell pool of TDOs, enhancing their proliferation and favoring a repopulation pattern similar to the one that is usually observed *in vivo*. Our findings are in line with previous works showing that cancer-derived ECM sustains the proliferation and invasion of CRC cell lines [33].

Scaffolds deriving from neoplastic peritoneum showed greater rigidity than those derived from normal peritoneum (Fig. 4D-F). The increased rigidity and crosslinking of the perilesional ECM was identified as an environmental modification predisposing CRC invasion [21]. The observed stiffening of the neoplastic ECM can be partially attributed to the more compact fine structure of the matrix and to the linearization of the fibers into bundles, as observed in Nebuloni et al. [21]. The increased amount of GAG in the perilesional ECM can also be related to the increase of the rigidity. Some authors have highlighted the relation between GAG and matrix stiffness: negatively charged GAG provide a repulsive force opposing compression and shear in the ECM [34]; moreover, GAG

bioRxiv preprint doi: https://doi.org/10.1101/2021.07.15.452437; this version posted July 15, 2021. The copyright holder for this preprint (which was not certified by peer review) is the author/funder. All rights reserved. No reuse allowed without permission.

capacity to retain high amounts of water and hydrated cations confers resistance to compressive forces [34].

The rigidity of healthy tissues increases with the age of the patient [35]. The relative stiffening in neoplastic tissues seems to be related to the aggressiveness of the cancer, which, in our study, was greater in the younger patient (Supplementary Fig. S3A), confirming that tumor stiffness favors its metastatic spread [36]. The high amount of GAGs observed in the neoplastic tissues could be a result of the metastatic transformation. In fact, chondoritin-sulfate is the main binding site for the isoform ν of CD44, which is a key player in the metastatic dissemination [37]. Transcriptome analysis also confirmed higher expression of GAGs in the repopulated neoplastic 3D-dEMCs. Further experiments will be performed with more donors to confirm the observed trends. The mechanical properties of the ECM could be involved in the direct reprogramming of the epithelial cells, conferring neoplastic features via the interactions between YAP/TAZ and specific oncogene aberrations such as RAS signalling [38]. However, GSEA analysis of genes from the YAP/TAZ signaling did not show an enrichment of this specific pathway in the repopulated matrices (data not shown).

Expression of specific genes that are fundamental for tissue architecture and stiffness, ECM remodelling, fibril generation, epithelial cell differentiation, resistance to compression and regulation of angiogenesis [39, 40, 41, 42, 43] was higher in 3D-dECMs generated from neoplastic tissue compared with 3D-dECMs generated from normal tissue or Matrigel (Fig. 7D and 7E), confirming the ability of our model to reproduce the PM microenvironment. Morphological and topographical experiments showed that the neoplastic scaffold undergoes complex structural modifications that enhance TDO adhesion and proliferation. In support of this concept, both normal and tumor 3D-dECMs showed an upregulation of genes involved in zinc and cooper metabolism and homeostasis, which was higher in the neoplastic-derived peritoneal matrix. These metal ions are involved in the regulation and activation of the metalloproteinase enzymes, which are the main modulators of the ECM through a proteolytic activity [44] and could play a role in the activation of

bioRxiv preprint doi: https://doi.org/10.1101/2021.07.15.452437; this version posted July 15, 2021. The copyright holder for this preprint (which was not certified by peer review) is the author/funder. All rights reserved. No reuse allowed without permission.

ECM remodeling pathways underlying the metastatic niche. All these observations make our model more attractive than the conventional culture methods with collagen-based scaffolds, which do not mimic real tissue conditions.

Transcriptomic analyses showed that repopulated 3D-dECMs presented features typical of the PM disease [45, 46] and expressed genes involved in ECM remodelling, such as NABA Matrisome and stem cell-related genes, ECM regulators and genes involved in the response to cytokine and pro-inflammatory stimuli, integrin interactions and collagen/proteoglycans modifications. These pathways were less represented in normal 3D-dECMs and absent in Matrigel samples, confirming a previous study showing that growth on the ECM of normal colon organoids transfected with mutant *APC* induces features typically associated with CRC progression [12]. The deregulation of genes belonging to pathways involved in the metastatic process, linked to metastatic spread and the development of the metastatic niche [5, 47], is in agreement with the fact that our organoids derive from metastatic lesions, where the cells activate a series of pathways to better adapt to the niche.

HIPEC simulation experiments highlighted the potential role of the neoplastic ECM in the development of drug resistance. Transcriptomic data indicated the activation of mechanisms correlated with drug resistance along with the modification of the mechanical properties of the ECM. In fact, growth on scaffolds increased the expression of anti-apoptotic and pro-survival genes, as well as genes involved in resistance to platin-based drugs. High expression of stiffness-related genes was also observed (Fig. 7F). The treatment response of the TDOs reflects the characteristics of the patient of origin, highlighting how PM-derived organoids could be used as patient avatars for personalized treatment. The engineered model we propose could therefore be a drug screening tool that more faithfully recapitulates the tumor microenvironment and response to treatment for tailored therapies than the classical monoculture 2D models, or even 3D-cultures, which are still being used [48].

However, the model presents some limitations, as it still does not reach a resolution level that allows it to mimic the PM niche in all its constituents. In fact, other components of the

bioRxiv preprint doi: https://doi.org/10.1101/2021.07.15.452437; this version posted July 15, 2021. The copyright holder for this preprint (which was not certified by peer review) is the author/funder. All rights reserved. No reuse allowed without permission.

microenvironment play a fundamental role in the spread of PM [49, 50], such as immune surveillance and the vascular system [51, 52]. Further optimization of our model will, therefore, imply the reconstruction of a specialized physiological microenvironment by incorporating vascular networks, the immune system, as well as organ-specific microbes. Moreover, the replacement of patient-derived 3D-dECM with a synthetic support with the same biochemical and physical characteristics of the components of the decellularized matrix will improve the reproducibility and allow personalized drug screenings to be performed on TDOs.

Our 3D model could be used as a pre-clinical platform to study the role of tumor ECM in the development of the PM niche. The model represents a physiological tool that can aid the identification of key players in the metastatic development, and may allow the selection, in a biologically relevant setting, of new therapeutic strategies, also providing a new tool to boost the bench-to-bed-side process to improve patient care. Finally, the approach described here might be used to generate other types of *ex vivo* metastatic niches.

bioRxiv preprint doi: https://doi.org/10.1101/2021.07.15.452437; this version posted July 15, 2021. The copyright holder for this preprint (which was not certified by peer review) is the author/funder. All rights reserved. No reuse allowed without permission.

References

1. L. Herszenyi, Z. Tulassay
Epidemiology of gastrointestinal and liver tumors
Eur. Rev. Med. Pharmacol. Sci., 14 (4) (2010), pp. 249-258

2. D. Baratti, S. Kusamura, F. Pietrantonio, M. Guaglio, M. Niger, M. Deraco
Progress in treatments for colorectal cancer peritoneal metastases during the years 2010-2015. A systematic review
Crit. Rev. Oncol. Hematol., 100 (2016), pp. 209-222

3. T.D. Yan, D. Black, R. Savady, P.H. Sugarbaker
Systematic review on the efficacy of cytoreductive surgery combined with perioperative intraperitoneal chemotherapy for peritoneal carcinomatosis from colorectal carcinoma
J. Clin. Oncol., 24 (24) (2006), pp. 4011-4019

4. D. Jayne
Molecular biology of peritoneal carcinomatosis
Cancer Treat. Res., 134 (2007), pp. 21-33

5. L. Lemoine, P. Sugarbaker, K. Van der Speeten
Pathophysiology of colorectal peritoneal carcinomatosis: Role of the peritoneum
World J. Gastroenterol., 22 (34) (2016), pp. 7692-7707

6. H. Peinado, H. Zhang, I.R. Matei, B. Costa-Silva, A. Hoshino, G. Rodrigues, *et al.*
Pre-metastatic niches: organ-specific homes for metastases
Nat. Rev. Cancer, 17 (5) (2017), pp. 302-317

7. K. Ksiazek, J. Mikula-Pietrasik, R. Catar, G. Dworacki, M. Winckiewicz, M. Frydrychowicz,*et al.*
Oxidative stress-dependent increase in ICAM-1 expression promotes adhesion of colorectal and pancreatic cancers to the senescent peritoneal mesothelium
Int. J. Cancer, 127 (2) (2010), pp. 293-303

8. J. Mikula-Pietrasik, P. Uruski, A. Tykarski, K. Ksiazek
The peritoneal "soil" for a cancerous "seed": a comprehensive review of the pathogenesis of intraperitoneal cancer metastases
Cell. Mol. Life Sci., 75(3) (2018), pp. 509-525

9. J. Drost, H. Clevers
Organoids in cancer research
Nat. Rev. Cancer., 18 (7) (2018), pp. 407-418

10. M. Fujii, M. Shimokawa, S. Date, A. Takano, M. Matano, K. Nanki,*et al.*
A Colorectal Tumor Organoid Library Demonstrates Progressive Loss of Niche Factor Requirements during Tumorigenesis
Cell Stem Cell, 18 (6) (2016), pp. 827-838

11. F. Bozzi, A. Mogavero, L. Varinelli, A. Belfiore, G. Manenti, C. Caccia,*et al.*
MIF/CD74 axis is a target for novel therapies in colon carcinomatosis

bioRxiv preprint doi: https://doi.org/10.1101/2021.07.15.452437; this version posted July 15, 2021. The copyright holder for this preprint (which was not certified by peer review) is the author/funder. All rights reserved. No reuse allowed without permission.

J. Exp. Clin. Cancer Res., 36(1) (2017), pp. 16.

12. H.J. Chen, Z. Wei, J. Sun, A. Bhattacharya, D.J. Savage, R. Serda, *et al.*
A recellularized human colon model identifies cancer driver genes
Nat. Biotechnol., 34 (8) (2016), pp. 845-851.

13. L. Genovese, L. Zawada, A. Tosoni, A. Ferri, P. Zerbi, R. Allevi,*et al.* M
Cellular localization, invasion, and turnover are differently influenced by healthy and tumor-derived extracellular matrix
Tissue Eng. Part. A, 20 (13-14) (2014), pp. 2005-2018.

14. I. Ubink, W.J. van Eden, P. Snaebjornsson, N.F.M. Kok, J. van Kuik, W.M.U. van Grevenstein, *et al.*
Histopathological and molecular classification of colorectal cancer and corresponding peritoneal metastases
Br. J. Surg., 105 (2) (2018)**,** pp. e204-e211.

15. M. Indrieri, A. Podestà, G. Bongiorno, D. Marchesi, P. Milani
Adhesive-free colloidal probes for nanoscale force measurements: production and Characterization
Rev. Sci. Instrum., 82 (2) (2011)

16. M. Chighizola, L. Puricelli, L. Bellon, A. Podestà
Large colloidal probes for atomic force microscopy: Fabrication and calibration issues
J. Mol. Recognit., 34 (1) (2021), pp. e2879.

17. H.J. Butt, M. Jaschke
Calculation of thermal noise in atomic force microscopy
Nanotechnology, 6 (1) (1995)

18. J. Laurent, A. Steinberger, L. Bellon.
Functionalized AFM probes for force spectroscopy: eigenmode shapes and stiffness calibration through thermal noise measurements.
Nanotechnology, 7 (24) (22) (2013), pp. 225504.

19. J.L Hutter, J. Bechhoefer
Calibration of atomic-force microscope tips
Rev. of Sci. Intrum., 64 (1868) (1993)

20. H. Schillers, C. Rianna, J. Schäpe, T. Luque, H. Doschke, M. Wälte, *et al.*
Standardized Nanomechanical Atomic Force Microscopy Procedure (SNAP) for Measuring Soft and Biological Samples
Sci. Rep., 11;7(1) (2017), pp. 5117.

21. M. Nebuloni, L. Albarello, A. Andolfo, C. Magagnotti, L. Genovese, I. Locatelli, *et al.*
Insight On Colorectal Carcinoma Infiltration by Studying Perilesional Extracellular Matrix
Sci. Rep., 4 (6) (2016), pp. 22522.

22. L. Puricelli, M. Galluzzi, C. Schulte, A. Podestà, P. Milani

bioRxiv preprint doi: https://doi.org/10.1101/2021.07.15.452437; this version posted July 15, 2021. The copyright holder for this preprint (which was not certified by peer review) is the author/funder. All rights reserved. No reuse allowed without permission.

Nanomechanical and topographical imaging of living cells by atomic force microscopy with colloidal probes
Rev. Sci. Instrum., 86 (3) (2015), pp. 033705

23. E. Shimshoni , I. Adir, R. Afik, I. Solomonov, A. Shenoy, M. Adler, *et al.*
Distinct extracellular-matrix remodeling events precede symptoms of inflammation
Matrix Biol., s0945-053X (30) (2020), pp. 30103-7.

24. A. Dobin, C.A. Davis, F. Schlesinger, J. Drenkow, C. Zaleski, S. Jha, *et al.*
STAR: ultrafast universal RNA-seq aligner
Bioinformatics, 29(1) (2013), pp. 15-21.

25. H.A.N. Alshehri
Compare and Contrast of Differential Gene Expression Software Packages of RNA-Seq.
Computational Science and Computational Intelligence (CSCI).
Las Vegas, NV, USA: IEEE; 2018.

26. E.Y. Chen, C.M. Tan, Y. Kou, Q. Duan, Z. Wang, G.V. Meirelles, *et al.*
Enrichr: interactive and collaborative HTML5 gene list enrichment analysis tool
BMC Bioinformatics, 14 (2013), pp. 128.

27. A. Naba, K.R. Clauser, H. Ding, C.A. Whittaker, S.A. Carr, R.O. Hynes
The extracellular matrix: Tools and insights for the "omics" era
Matrix Biol., 49 (2016), pp. 10-24

28. I. Ubink, A.C.F. Bolhaqueiro, S.G. Elias, D.A.E. Raats, A. Constantinides, N.A. Peters,*et al.*
Organoids from colorectal peritoneal metastases as a platform for improving hyperthermic intraperitoneal chemotherapy
Br. J. Surg., 106 (10) (2019), pp. 1404-1414.

29. H. Weijing, R. El Botty, E. Montaudon, L. Malaquin, F. Deschaseaux, *et al.*
In vitro bone metastasis dwelling in a 3D bioengineered niche
Biomaterials, 269 (2021): 120624.

30. H. Cramer. ***Mathematical methods of statistics*** Princeton University Press, 1999.

31. M. Fujii, M. Matano, K. Nanki, T. Sato
Efficient genetic engineering of human intestinal organoids using electroporation
Nat. Protoc., 10 (10) (2015), pp. 1474-1485

32. X. Tian, M.E. Werner, K.C. Roche, A.D. Hanson, H.P. Foote, S.K. Yu, *et al.*
Organ-specific metastases obtained by culturing colorectal cancer cells on tissue-specific decellularized scaffolds
Nat. Biomed. Eng., 2 (2018), pp. 443-452.

33. E. D'Angelo, D. Natarajan, F. Sensi, O. Ajayi, M. Fassan, E. Mammano, *et al.*
Patient-Derived Scaffolds of Colorectal Cancer Metastases as an Organotypic 3D Model of the Liver Metastatic Microenvironment
Cancers (Basel), **12**(2) (2020)

bioRxiv preprint doi: https://doi.org/10.1101/2021.07.15.452437; this version posted July 15, 2021. The copyright holder for this preprint (which was not certified by peer review) is the author/funder. All rights reserved. No reuse allowed without permission.

34 M.D. Buschmann & A.J. Grodzinsky
A molecular model of proteoglycan-associated electrostatic forces in cartilage mechanics
J. Biomech. Eng., 117 (2) (1995), pp. 179-92

35. L.P. Ferreira, V.M. Gaspar, J.F. Mano
Decellularized Extracellular Matrix for Bioengineering Physiomimetic 3D in Vitro Tumor Models
Trends Biotechnol., 38 (12) (2020), pp. 1397-1414

36. J. Winkler, A. Abisoye-Ogunniyan, K.J. Metcalf, Z. Werb
Concepts of extracellular matrix remodelling in tumour progression and metastasis
Nat. Commun., 11 (1) (2020), pp. 5120

37. F. Zanconato, M. Cordenonsi, S. Piccolo
Y**AP and TAZ: a signalling hub of the tumour microenvironment**
Nat. Rev. Cancer, 19 (8) (2019), pp. 454-464

38. T. Panciera, A. Citron, D. Di Biagio, G. Battilana, A. Gandin, S. Giulitti, *et al.*
Reprogramming normal cells into tumour precursors requires ECM stiffness and oncogene-mediated changes of cell mechanical properties *Nat. Mater.*, 19 (7) (2020), pp. 797-806.

39. S.V. Glavey, A. Naba, S. Manier, K. Clauser, S. Tahri, J. Park, *et al.*
Proteomic characterization of human multiple myeloma bone marrow extracellular matrix
Leukemia, 31(11) (2017), pp. 2426-2434

40. K.A. Robinson, M. Sun, C.E. Barnum, S.N. Weiss, J. Huegel, S.S. Shetye, *et al.*
Decorin and biglycan are necessary for maintaining collagen fibril structure, fiber realignment, and mechanical properties of mature tendons *Matrix Biol.*, 64 (2017), pp. 81-93

41. H. Nistala, S. Lee-Arteaga, S. Smaldone, G. Siciliano, L. Carta, R.N. Ono, *et al.*
Fibrillin-1 and -2 differentially modulate endogenous TGF-beta and BMP bioavailability during bone formation.
J. Cell. Biol., 190 (6) (2010), pp. 1107-1121.

42. M. Schlesinger, G. Bendas
Vascular cell adhesion molecule-1 (VCAM-1) an increasing insight into its role in tumorigenicity and metastasis
Int. J. Cancer, 136 (11) (2015), pp. 2504-2514

43. K. Bajou, H. Peng, W.E. Laug, C. Maillard, A. Noel, J.M. Foidart, *et al.*
Plasminogen activator inhibitor-1 protects endothelial cells from FasL-mediated apoptosis
Cancer Cell, 14 (4) (2008), pp. 324-334.

44. W. Ceelen, R.G. Ramsay, V. Narasimhan, A.G. Heriot, O. De Wever
Targeting the Tumor Microenvironment in Colorectal Peritoneal Metastases
Trends Cancer, 6 (3) (2020), pp. 236-246

bioRxiv preprint doi: https://doi.org/10.1101/2021.07.15.452437; this version posted July 15, 2021. The copyright holder for this preprint (which was not certified by peer review) is the author/funder. All rights reserved. No reuse allowed without permission.

45. D.G. Jayne, S. Fook, C. Loi, F. Seow-Choen
Peritoneal carcinomatosis from colorectal cancer
Br. J. Surg., 89 (12) (2002), pp. 1545-1550

46. R. Siegel, C. Desantis, A. Jemal.
Colorectal cancer statistics, 2014
CA Cancer. J. Clin., 64 (2) (2014), pp. 104-117

47. S. Varghese, M. Burness, H. Xu, T. Beresnev, J. Pingpank, H.R. Alexander
Site-specific gene expression profiles and novel molecular prognostic factors in patients with lower gastrointestinal adenocarcinoma diffusely metastatic to liver or peritoneum
Ann. Surg. Oncol., 14 (12) (2007), pp. 3460-3471

48. C.M. Ghajar
Metastasis prevention by targeting the dormant niche
Nat. Rev. Cancer, 15 (4) (2015), pp. 238-247

49. M. Bleijs, M. van de Wetering, H. Clevers, J. Drost
Xenograft and organoid model systems in cancer research
EMBO J., 38 (15) (2019), pp. e101654.

50. G.S. Hussey, T.J. Keane, S.F. Badylak
The extracellular matrix of the gastrointestinal tract: a regenerative medicine platform
Nat. Rev. Gastroenterol. Hepatol., 14 (9) (2017)**,** pp. 540-552

51. C.T. Seebauer, S. Brunner, G. Glockzin, P. Piso, P. Ruemmele, H.J. Schlitt, *et al.*
Peritoneal carcinomatosis of colorectal cancer is characterized by structural and functional reorganization of the tumor microenvironment inducing senescence and proliferation arrest in cancer cells
Oncoimmunology, 5 (12) (2016), pp. e1242543.

52. L. Mohrmann, M.K. Zowada, H. Strakerjahn, C. Siegl, A. Kopp-Schneider, D. Krunic, *et al.*
A perivascular niche in the bone marrow hosts quiescent and proliferating tumorigenic colorectal cancer cells
Int. J. Cancer., 147 (2) (2020), pp. 519-531.

Acknowledgements

The authors wish to thank the Imaging Technological Development Unit (TDU) of the FIRC Institute of Molecular Oncology, IFOM, Milan, Italy and the DNA Sequencing Facility of Cogentech Ltd, Benefit Corporation with a Sole Shareholder, Milan, Italy. In particular, we would like to thank Sara Volorio, Mirko Ribone and Claudia Valli from Cogentech Ltd, Benefit Corporation wih a Sole Shareholder, Milan, Italy, Oscar Illescas Pomposo for helping us in TDO

bioRxiv preprint doi: https://doi.org/10.1101/2021.07.15.452437; this version posted July 15, 2021. The copyright holder for this preprint (which was not certified by peer review) is the author/funder. All rights reserved. No reuse allowed without permission.

mainteinance and development. The authors express their gratitude to Wessen Maruwge, an English author's editor in Milan, for revising the manuscript.

Author contributions

L.V., S.B. designed and performed all the experiments and edited the manuscript. L.V., M.G1., M.G2 and M.A.P., conceived and design the study. M.C., A.O., and A.P., performed AFM analysis and edited the manuscript. A.O., E.C., and D. P., aided all the imaging acquisition. F. Z., and F. I., performed all the bioinformatics analyses and critically discussed the data. S.Z., S. P. M., and S. F., performed RNA-seq and NGS experiments. M.G1., K.S., D.B., and M.D., performed surgical intervention and collected human samples. M.F., and G.G., performed IHC and HC analyses. L.C., and M.M., selected the cases and interpreted IHC and HC analyses. A.B., aided in generating organoids. M.V., aided in the transcirptomics data interpretation. L.V., M.G1., M.G2., A.P., and M.A.P., wrote the manuscript. L.V., S.Z. M.G2., and M.A.P., critically read the manuscript

Competing interests

The authors declare no competing interests.

Fundings

Funds obtained through an Italian law that allows taxpayers to allocate 0.5 percent of their tax to a research institution of their choice.

bioRxiv preprint doi: https://doi.org/10.1101/2021.07.15.452437; this version posted July 15, 2021. The copyright holder for this preprint (which was not certified by peer review) is the author/funder. All rights reserved. No reuse allowed without permission.

Figure legends

Fig. 1. Diagram of established method. (A) Schematic representation of the protocol used to develop CRC PM-derived organoids. Digested cells were cultured in presence of different growth factors, to mimic different niche factors conditions. (**ENA:** human EGF recombinant protein (**E**); human Noggin recombinant protein (**N**); A83-01, anti-p38 inhibitor (**A**); **ENAS:** ENA supplemented with SB201290 anti-Rock inhibitor (**S**); **WR+/-:** cell culture media supplemented with or without human Wnt3A recombinant protein (**W**) and human R-Spondin-1 recombinant protein (**R**)). Organoids developed under a specific culture medium condition, depending on the growth factors they needed. **(B)** Schematic representation of the protocol used to obtain peritoneal-derived 3D-dECMs. **(C)** Experimental design used to develop the *ex vivo* 3D-engineered PM lesions. **(D)** Workflow chart representing the experimental design used to reproduce *in vitro* HIPEC treatments (**UNT:** untreated group; **CTRL:** control group (mitomycin-c vehicle: physiological solution); **HIPEC:** Hyperthermic Intraperitoneal Chemotherapy; **TDO:** tumor-derived organoid; **IF:** Immunofluorescence; **IHC:** Immunohistochemistry).

Fig. 2. Establishment and characterization of human peritoneal metastases (PM)-derived organoids. (A) Comparative histological and IHC analysis of PM-derived organoids and their tissue of origin, using H&E staining and CK AE1/AE3, CK20, CK19, CDX2, and Ki-67 immunostaining. PM-derived organoids retain the main features of their tissue of origin. PM tissues generally present a tumor epithelium surrounded by stromal-derived cells, while organoids consist exclusively of epithelial cells. Scale bar: 100 µm. **(B)** Bright-field images depicting PM-derived organoid phenotypes. The left micrograph shows a glandular-like branched organoid, while the right one shows a spherical-like cohesive organoid. Scale bar: 100 µm. **(C)** IHC analysis of PM-derived organoids (top) and their tissue of origin (bottom), using LGR5 immunostaining. LGR5-positive cells found in PM tissue are retained in the derived organoids. Scale bar: 100 µm. **(D)**

bioRxiv preprint doi: https://doi.org/10.1101/2021.07.15.452437; this version posted July 15, 2021. The copyright holder for this preprint (which was not certified by peer review) is the author/funder. All rights reserved. No reuse allowed without permission.

Summary of cancer-related genes, analyzed by target DNA sequencing, with acquired mutations in TDOs with respect to their tumor of origin (red boxes). The percentage of similarity was reported. Passage numbers of the organoid lines were: C1: P11; C2: P13; C3: P10; C4: P14; C6: P10.

Fig. 3. Establishment of 3D-dECM scaffolds from peritoneal cavity. (A) DNA quantification of normal and neoplastic peritoneal tissue samples before (fresh) and after the decellularization treatment (dECM), showing a high DNA depletion. Student's *t-test* (***p<0.001). **(B)** IF analysis of normal and neoplastic peritoneal samples before and after the decellularization procedure using the WGA (Wheat Germ Agglutinin, a marker for glycoproteins in lipid membranes; red) antibody. The samples were counterstained with DAPI (blue). Scale bar: 100 µm. **(C)** IHC analysis of fresh peritoneal-derived tissues and the corresponding decellularized samples using H&E staining and vimentin, pan-Cytokeratin (CK AE1/AE3), and collagen-IV immunostaining. Scale bar: 200 µm. **(D)** Van Gienson, Masson's Trichrome and Alcian-PAS stains for the detection of collagens, polysaccharides, glycoproteins, and structural tissue preservation on fresh and decellularized peritoneal-derived samples. Scale bar: 200 µm.

Fig. 4. Morphological and mechanical properties of PM-derived 3D-dECMs. (A) Confocal and polarized light microscopy representative images of peritoneal-derived 3D-dECMs samples. Scale bar: 50 µm. **(B)** AFM topography representative images of peritoneal-derived 3D-dECMs. Phase, height and peak force error images of both normal and neoplastic decellularized matrices are shown. Scale bar: 1 µm. **(C)** Quantification of collagens I/IV and sulphated glycosaminoglycans (sGAG) on fresh and decellularized peritoneal tissues. Student's *t-test* (***p<0.001 and **p<0.01). **(D)** Distribution of the YM values obtained for each patient (Pt) and condition (Normal and Neoplastic). Box plots: each dot represents the YM value from a single FC; the quartile group, outliers and median values are highlighted. **(E)** Result of the statistical analysis of the YM value for each patient and condition tested. The bars and error bars represent the mean median YM values

bioRxiv preprint doi: https://doi.org/10.1101/2021.07.15.452437; this version posted July 15, 2021. The copyright holder for this preprint (which was not certified by peer review) is the author/funder. All rights reserved. No reuse allowed without permission.

and the effective SEMs, respectively, calculated as described in Materials and Methods. **(F)** Results of the statistical analysis presented in e, normalized to the YM value of the normal condition.

Fig. 5. Peritoneum-derived 3D-dECM scaffolds support colonization, infiltration and proliferation of PM-derived organoids, maintaining the stem cell pool. **(A)** H&E staining of decellularized matrices derived from normal (top) or neoplastic (bottom) peritoneum repopulated with PM-derived organoids (C1) as indicated. Scale bar: 50 µm. The repopulation experiments were performed in triplicate. **(B)** IF analysis of 3D decellularized matrices derived from normal (top) and neoplastic (bottom) peritoneum repopulated with PM-derived organoids (C1) using Ki-67$^+$ (green) and collagen IV$^+$ (red) antibodies as indicated. The samples were counterstained with DAPI (blue). Scale bar: 20 µm. **(C)** Proliferation rate of PM-derived organoids measured as the percentage of Ki-67$^+$ cells present in fields devoid of dead cells. Five fields per experiment (40X magnification) were counted. Data are presented as median and SD for surgical specimens of three patients. One-way ANOVA (***p<0.001). **(D)** IF analysis of 3D decellularized matrices derived from normal (top) and neoplastic (bottom) peritoneum repopulated with PM-derived organoids (C1) using LGR5$^+$ (green) and collagen IV$^+$ (red) antibodies as indicated. The samples were counterstained with DAPI (blue). Scale bar: 20 µm. **(E)** Amount of stem cells in PM-derived organoids, measured as the percentage of LGR5$^+$ cells present in fields devoid of dead cells. Five fields per experiment (40X magnification) were counted. Data are presented as median and SD for surgical specimens of three patients. One-way ANOVA (**p<0.01).

Fig. 6. *ex vivo* engineered PM lesions are comparable to PMs found *in vivo*. (A) Comparative histological and immunohistochemical images of PM-derived organoids (C1) versus their corresponding tumor of origin and the *ex vivo* engineered PM lesion. Samples were analyzed for the expression of the CRC-specific markers: CK AE1/AE3, CK19, CK20, CDX2, and Mib-1. Scale bar: 100 µM. Images in the first two lanes were previously published (20). **(B)** Histological

bioRxiv preprint doi: https://doi.org/10.1101/2021.07.15.452437; this version posted July 15, 2021. The copyright holder for this preprint (which was not certified by peer review) is the author/funder. All rights reserved. No reuse allowed without permission.

comparison of peritoneal metastasis and neoplastic-derived 3D-dECMs repopulated with PM-derived organoids (C1). The *ex vivo* engineered PM lesions present histological features that are typical of PMs of gastrointestinal origin. Scale bar: 20 µm.

Fig. 7. Gene expression analysis of engineered PM lesions. (A) Percentage of up- and down-regulated genes belonging to the Matrisome dataset, in organoids grown on 3D-dECMs compared to Matrigel or in neoplastic versus normal 3D-dECM. **(B)** Unsupervised hierarchical clustering of the organoids according to the expression of the top DEGs included in Naba Secreted Factors and in Naba Collagens categories. **(C)** Fold changes of genes belonging to the indicated gene sets among the top 100 deregulated genes. Gene ranks for relative fold change are shown on the x-axis and the logFCs on the y-axis. **(D)** Box plot showing the expression of genes selected for their involvement in the indicated processes of the Naba Matrisome datasets. Median and interquartile range are displayed as horizontal lines. Black squares in the bottom panel indicate which category the genes belong to. **(E)** Expression of genes selected for their involvement in the indicated processes of GO BP and KEGG databases. Median and interquartile range are displayed as horizontal lines. Black squares in the bottom panel indicate which category the genes belong to. **(F)** Expression of genes selected for their involvement in the indicated processes, using a selection of genes related to the following biological processes: cell-cell/cell-matrix interactions, extracellular matrix stiffness and drug resistance. Median and interquartile range are displayed as horizontal lines. Black squares in the bottom panel indicate which category the genes belong to.

Fig. 8. 3D-dECM scaffolds decrease the efficacy of HIPEC treatments. (A) IHC analysis of C1 and C3 PM-derived organoids cultured in Matrigel and on neoplastic-derived peritoneal 3D-dECMs, after *in vitro* HIPEC treatments, using Ki-67 immunostaining. Scale bar: 50 µm. **(B)** IF analysis of C1 and C3 PM-derived organoids cultured in Matrigel and on neoplastic-derived peritoneal 3D-dECMs, after HIPEC treatments, using cCASPASE-3 antibody (green). The samples

bioRxiv preprint doi: https://doi.org/10.1101/2021.07.15.452437; this version posted July 15, 2021. The copyright holder for this preprint (which was not certified by peer review) is the author/funder. All rights reserved. No reuse allowed without permission.

were counterstained with WGA (red) and DAPI (blue). Scale bar: 20 µm. **(C)** Proliferation rate of PM-derived organoids (C1, left panel; C3, right panel) measured as the percentage of Ki-67^{+} cells present in fields devoid of dead cells. Five fields per experiment (40X magnification) were counted. Data are presented as median and SD for surgical specimens of three patients. One-way ANOVA (**p<0.01). **(D)** Percentage of apoptotic PM-derived organoids (C1, left panel; C3, right panel) measured as the percentage of cCASPASE-3^{+} cells present in selected fields. Five fields per experiment (40X magnification) were counted. Data are presented as median and SD for surgical specimens of three patients. One-way ANOVA (**p<0.01).

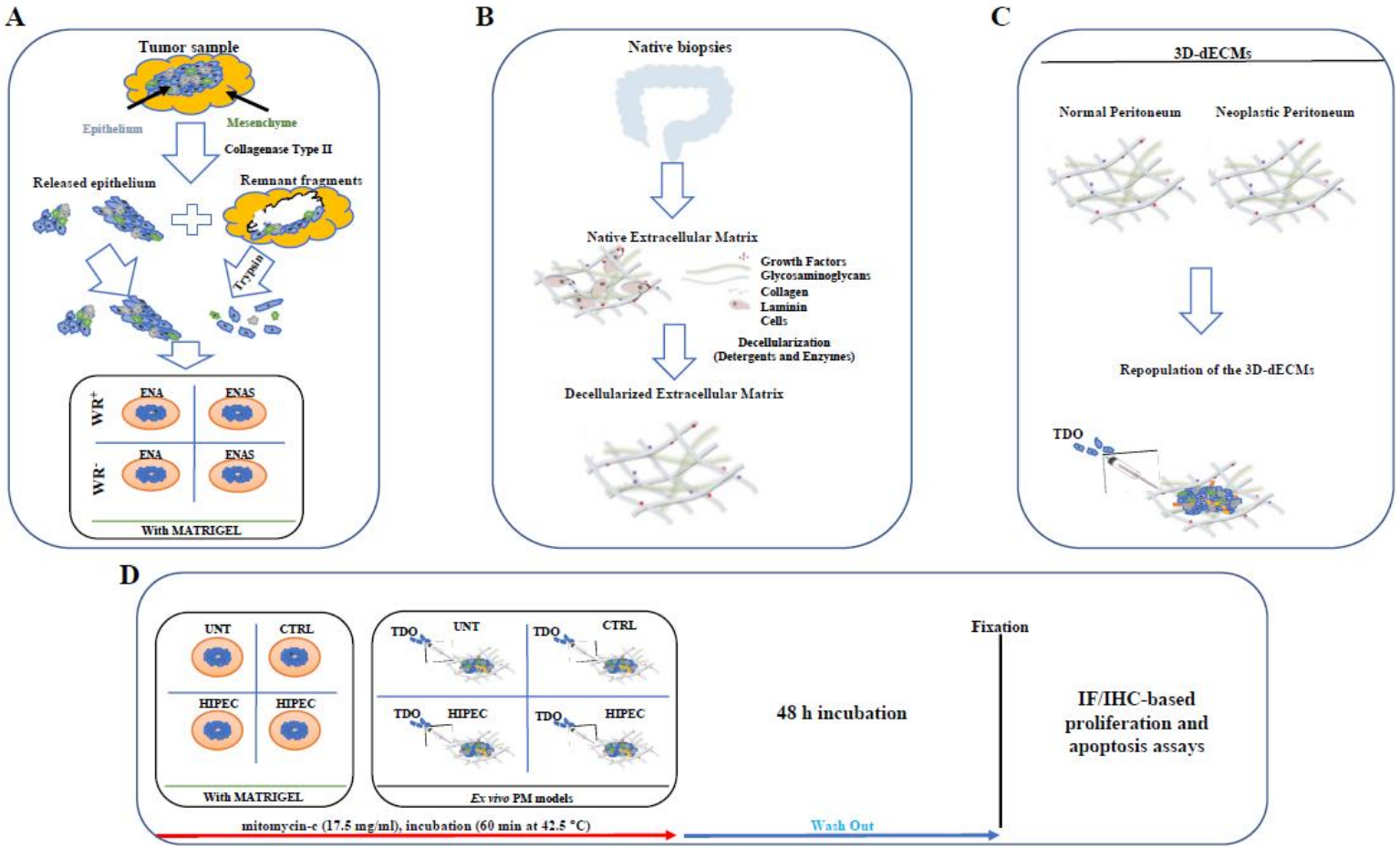
A
Tumor sample
Epithelium
Mesenchyme
Collagenase Type II
Released epithelium
Remnant fragments
Trypsin
WR+
WR-
ENA
ENAS
ENA
ENAS
With MATRIGEL
B
Native biopsies
Native Extracellular Matrix
Growth Factors
Glycosaminoglycans
Collagen
Laminin
Cells
Decellularization
(Detergents and Enzymes)
Decellularized Extracellular Matrix
C
3D-dECMs
Normal Peritoneum
Neoplastic Peritoneum
Repopulation of the 3D-dECMs
TDO
D
UNT
CTRL
HIPEC
HIPEC
With MATRIGEL
TDO
UNT
TDO
CTRL
TDO
HIPEC
TDO
HIPEC
Ex vivo PM models
48 h incubation
Fixation
IF/IHC-based
proliferation and
apoptosis assays
mitomycin-c (17.5 mg/ml), incubation (60 min at 42.5 °C)
Wash Out

Figure 1

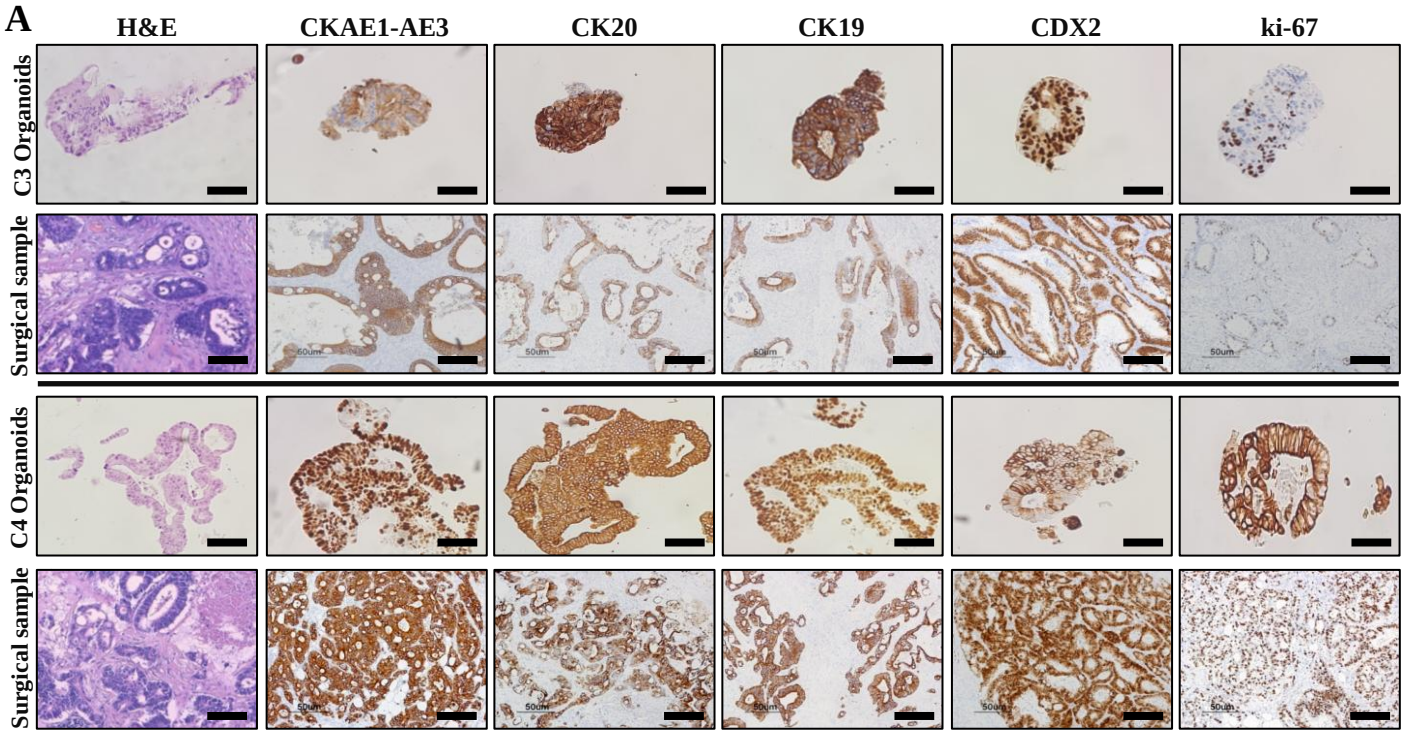

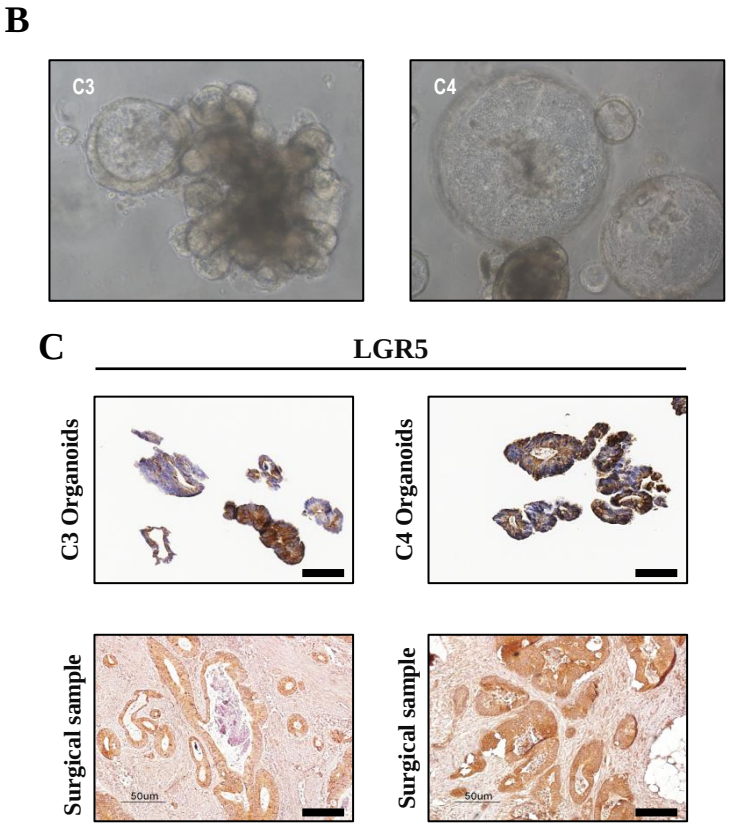

D

	C1	C2	C3	C4	C6
% of Similarity	97,92	91,84	100	87,18	93,85
APC					■
ATM		■			
BARD1		■		■	
BMPR1A					
BRAF					
BRCA1					
BRCA2					
BRIP1					
CDH1					
CDKN2A					
CHEK2					
CTNNA1					
EGFR					
ERBB2					
FANCM					
KRAS					■
MLH1					
MSH2					
MSH3				■	
MSH6				■	
MUTYH					
NBN					
PALB2					
PIK3CA					
PMS2		■			
POLD1					
POLE					
RAD51C	■				
RAD51D					
SMAD4					■
TP53		■			■

Figure 2

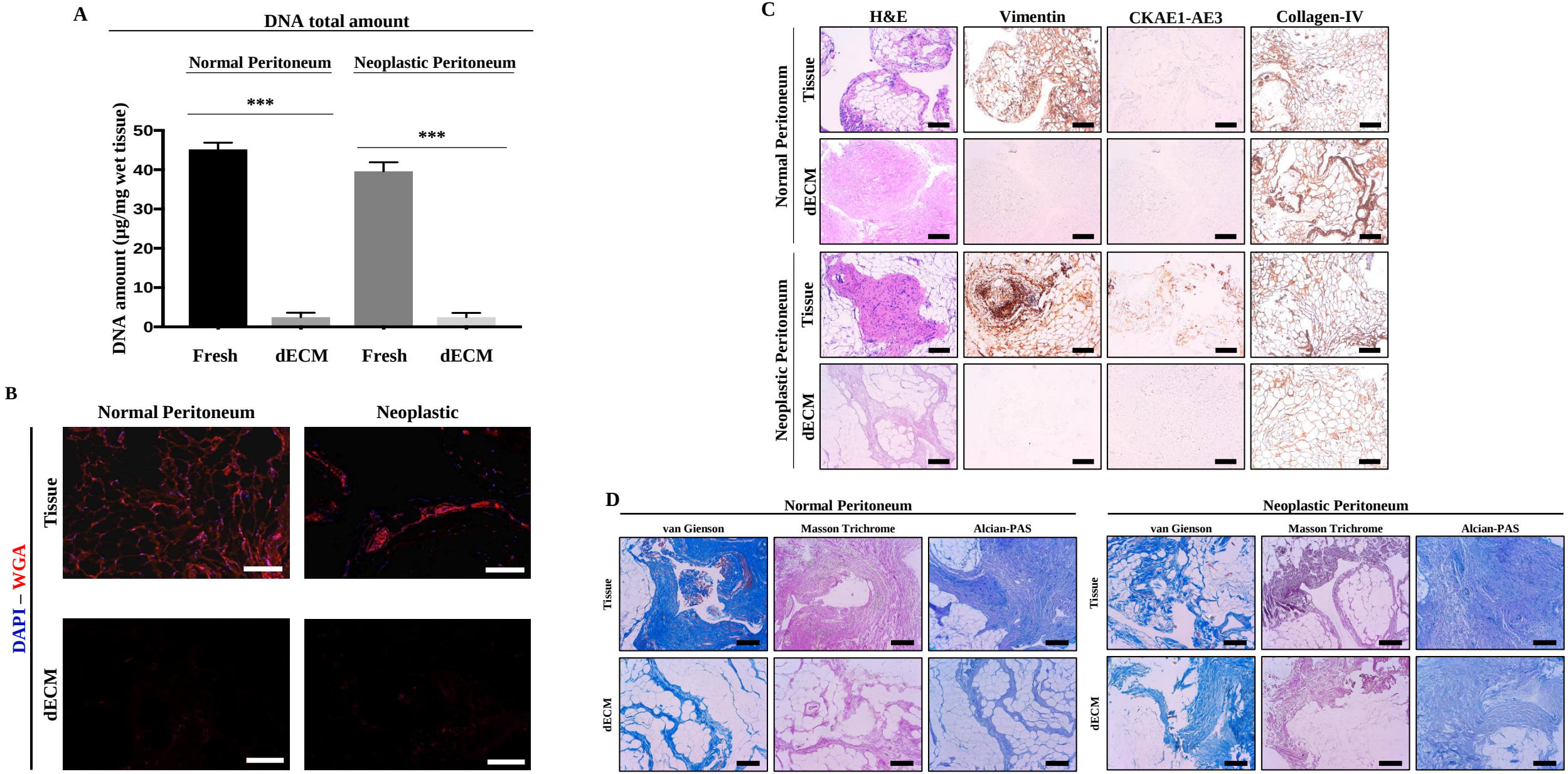
A
DNA total amount
Normal Peritoneum
Neoplastic Peritoneum
***
***
DNA amount (µg/mg wet tissue)
50
40
30
20
10
0
Fresh
dECM
Fresh
dECM
B
Normal Peritoneum
Neoplastic
Tissue
dECM
DAPI – WGA
C
H&E
Vimentin
CKAE1-AE3
Collagen-IV
Normal Peritoneum
Tissue
dECM
Neoplastic Peritoneum
Tissue
dECM
D
Normal Peritoneum
Neoplastic Peritoneum
van Gienson
Masson Trichrome
Alcian-PAS
Tissue
dECM

Figure 3

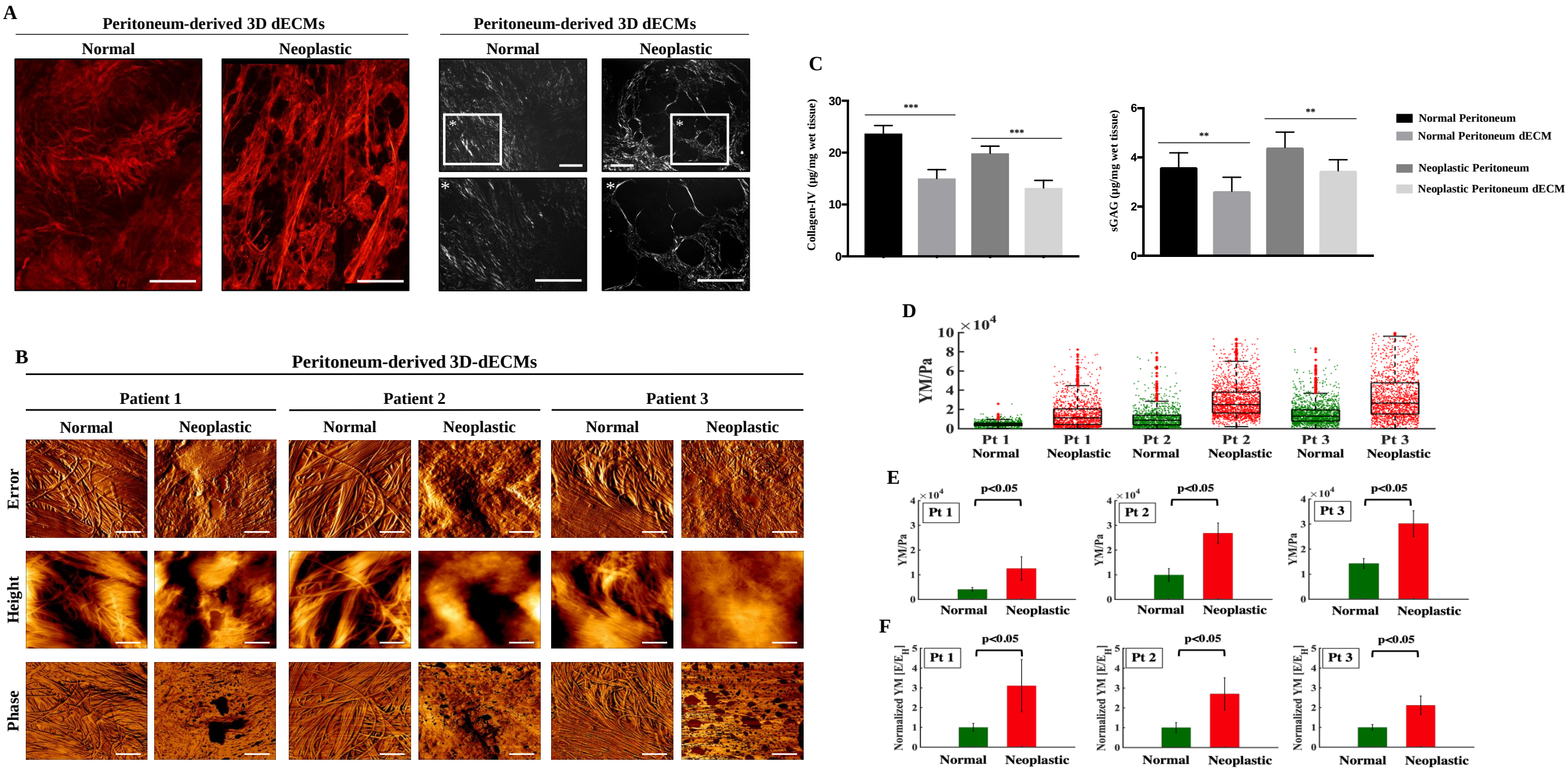
A
Peritoneum-derived 3D dECMs
Normal
Neoplastic
Peritoneum-derived 3D dECMs
Normal
Neoplastic
B
Peritoneum-derived 3D-dECMs
Patient 1
Patient 2
Patient 3
Normal
Neoplastic
Normal
Neoplastic
Normal
Neoplastic
Error
Height
Phase
C
Collagen-IV (µg/mg wet tissue)
sGAG (µg/mg wet tissue)
***
***
**
**
Normal Peritoneum
Normal Peritoneum dECM
Neoplastic Peritoneum
Neoplastic Peritoneum dECM
D
YM/Pa
×10^4
Pt 1 Normal
Pt 1 Neoplastic
Pt 2 Normal
Pt 2 Neoplastic
Pt 3 Normal
Pt 3 Neoplastic
E
Pt 1
Pt 2
Pt 3
p<0.05
YM/Pa
Normal
Neoplastic
F
Pt 1
Pt 2
Pt 3
p<0.05
Normalized YM [E/E_H]
Normal
Neoplastic

Figure 4

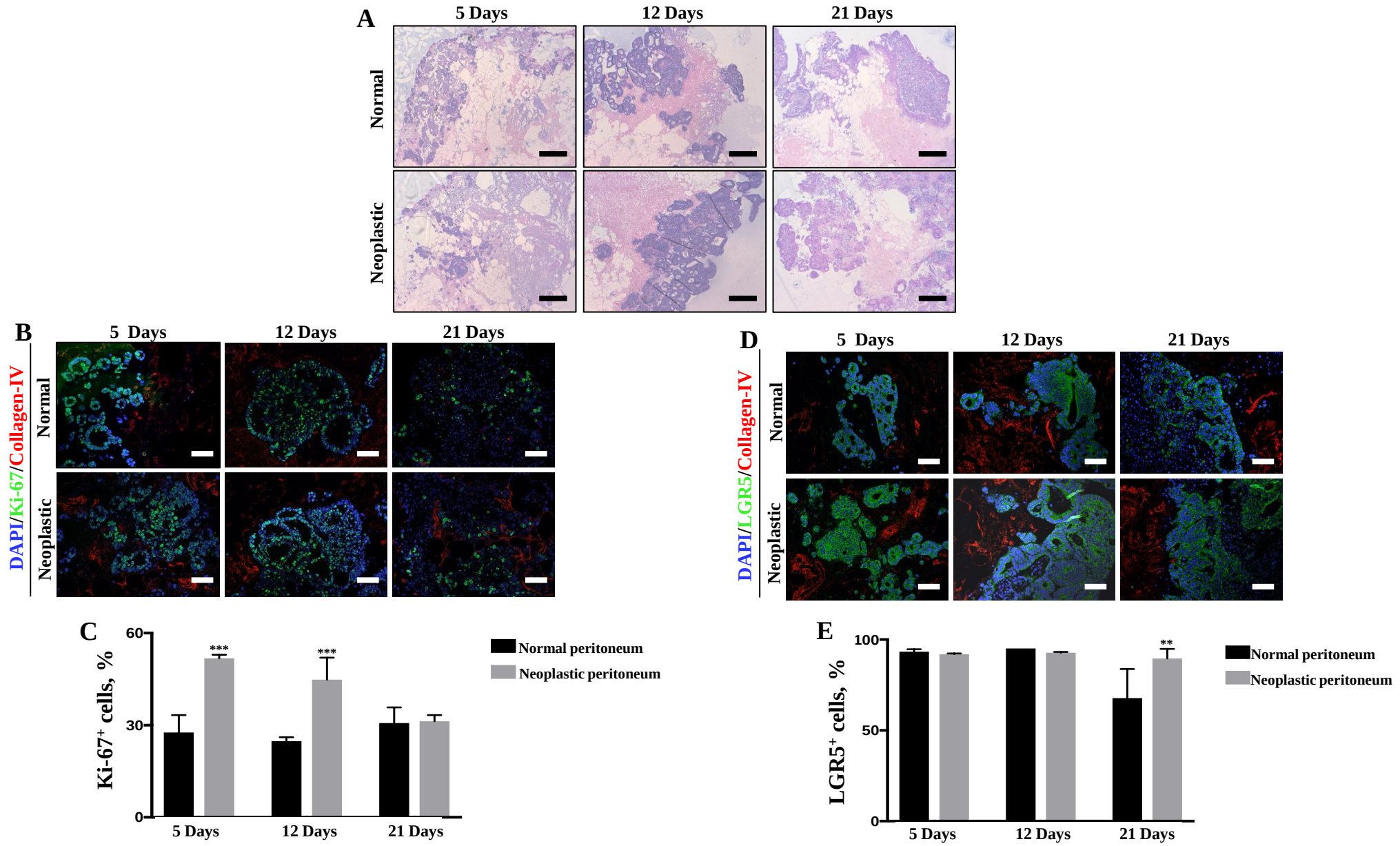
A
5 Days
12 Days
21 Days
Normal
Neoplastic
B
5 Days
12 Days
21 Days
DAPI/Ki-67/Collagen-IV
Normal
Neoplastic
D
5 Days
12 Days
21 Days
DAPI/LGR5/Collagen-IV
Normal
Neoplastic
C
Ki-67+ cells, %
60
30
0
***
***
5 Days
12 Days
21 Days
Normal peritoneum
Neoplastic peritoneum
E
LGR5+ cells, %
100
50
0
**
5 Days
12 Days
21 Days
Normal peritoneum
Neoplastic peritoneum

Figure 5

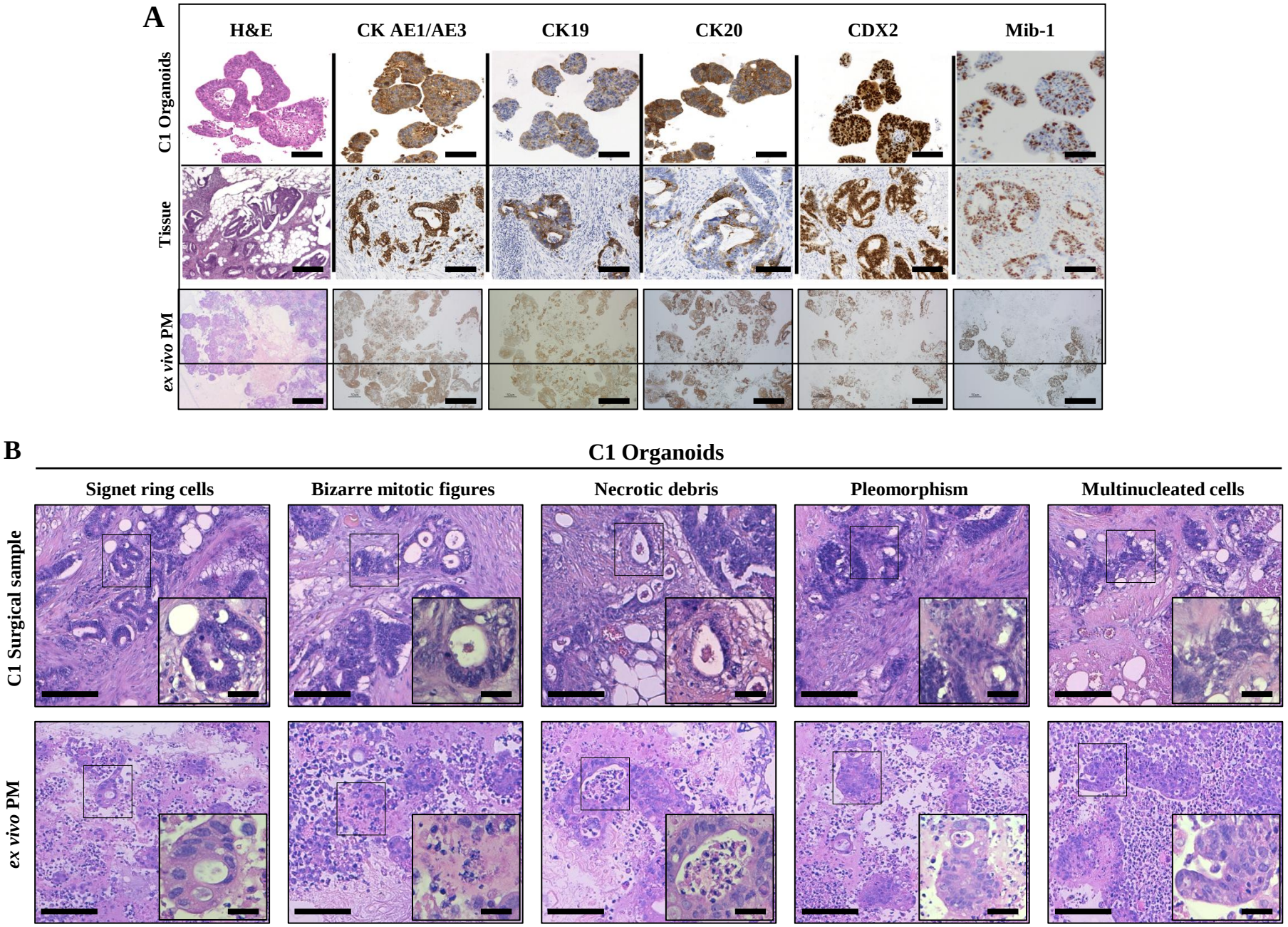
A
H&E
CK AE1/AE3
CK19
CK20
CDX2
Mib-1
C1 Organoids
Tissue
ex vivo PM
B
C1 Organoids
Signet ring cells
Bizarre mitotic figures
Necrotic debris
Pleomorphism
Multinucleated cells
C1 Surgical sample
ex vivo PM

Figure 6

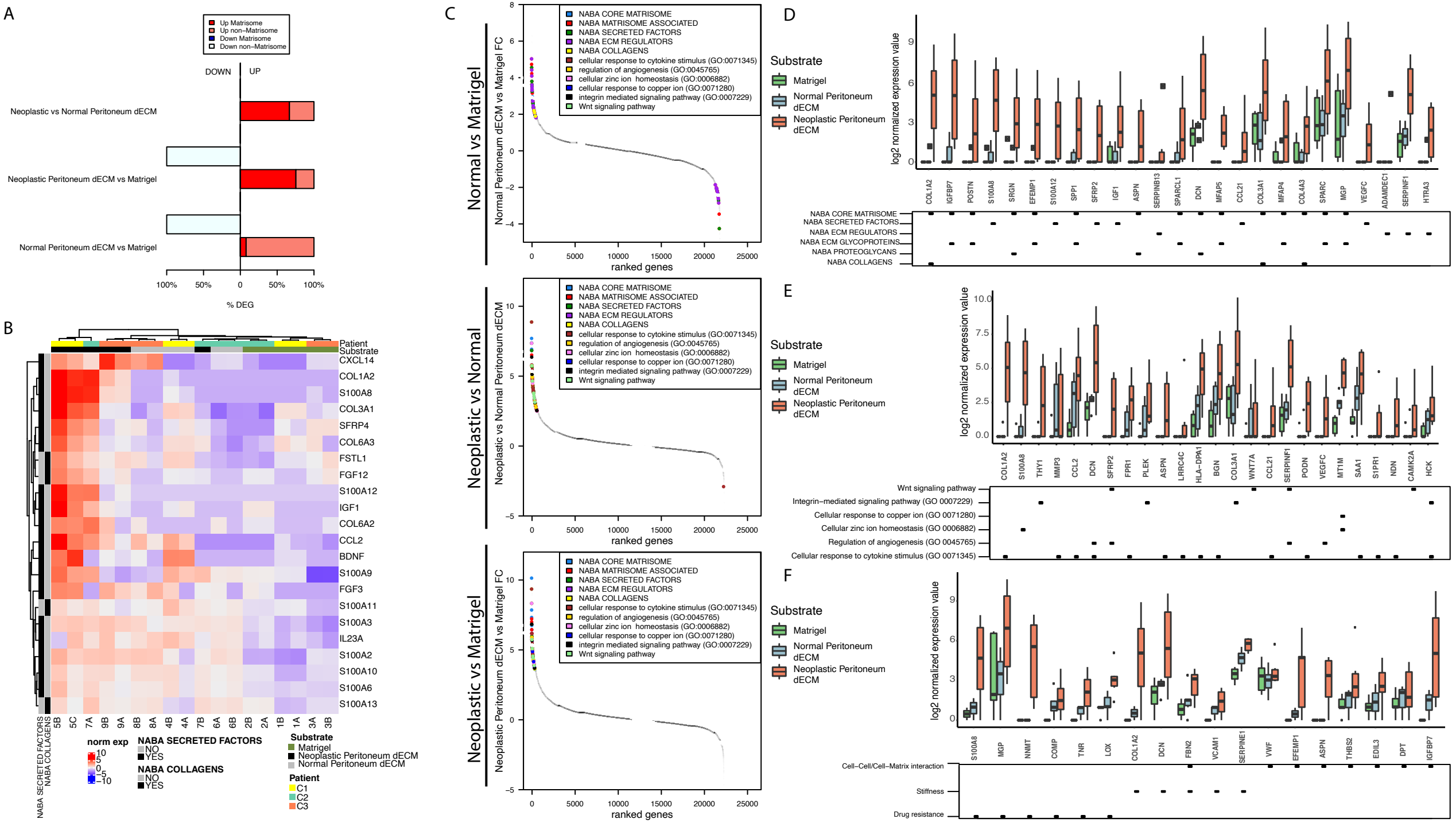
A
Up Matrisome
Up non–Matrisome
Down Matrisome
Down non–Matrisome
DOWN
UP
Neoplastic vs Normal Peritoneum dECM
Neoplastic Peritoneum dECM vs Matrigel
Normal Peritoneum dECM vs Matrigel
100%
50%
0
50%
100%
% DEG
B
Patient
Substrate
CXCL14
COL1A2
S100A8
COL3A1
SFRP4
COL6A3
FSTL1
FGF12
S100A12
IGF1
COL6A2
CCL2
BDNF
S100A9
FGF3
S100A11
S100A3
IL23A
S100A2
S100A10
S100A6
S100A13
5B 5C 7A 9B 9A 8B 8A 4B 4A 7B 6A 6B 2B 2A 1B 1A 3A 3B
NABA SECRETED FACTORS
NABA COLLAGENS
norm exp
10
5
0
−5
−10
NABA SECRETED FACTORS
NO
YES
NABA COLLAGENS
NO
YES
Substrate
Matrigel
Neoplastic Peritoneum dECM
Normal Peritoneum dECM
Patient
C1
C2
C3
C
Normal vs Matrigel
Normal Peritoneum dECM vs Matrigel FC
Neoplastic vs Normal
Neoplastic vs Normal Peritoneum dECM
Neoplastic vs Matrigel
Neoplastic Peritoneum dECM vs Matrigel FC
NABA CORE MATRISOME
NABA MATRISOME ASSOCIATED
NABA SECRETED FACTORS
NABA ECM REGULATORS
NABA COLLAGENS
cellular response to cytokine stimulus (GO:0071345)
regulation of angiogenesis (GO:0045765)
cellular zinc ion homeostasis (GO:0006882)
cellular response to copper ion (GO:0071280)
integrin mediated signaling pathway (GO:0007229)
Wnt signaling pathway
ranked genes
D
Substrate
Matrigel
Normal Peritoneum dECM
Neoplastic Peritoneum dECM
log2 normalized expression value
COL1A2 IGFBP7 POSTN S100A8 SRGN EFEMP1 S100A12 SPP1 SFRP2 IGF1 ASPN SERPINB13 SPARCL1 DCN MFAP5 CCL21 COL3A1 MFAP4 COL4A3 SPARC MGP VEGFC ADAMDEC1 SERPINF1 HTRA3
NABA CORE MATRISOME
NABA SECRETED FACTORS
NABA ECM REGULATORS
NABA ECM GLYCOPROTEINS
NABA PROTEOGLYCANS
NABA COLLAGENS
E
Substrate
Matrigel
Normal Peritoneum dECM
Neoplastic Peritoneum dECM
log2 normalized expression value
COL1A2 S100A8 THY1 MMP3 CCL2 DCN SFRP2 FPR1 PLEK ASPN LRRC4C HLA–DPA1 BGN COL3A1 WNT7A CCL21 SERPINF1 PODN VEGFC MT1M SAA1 S1PR1 NDN CAMK2A HCK
Wnt signaling pathway
Integrin–mediated signaling pathway (GO 0007229)
Cellular response to copper ion (GO 0071280)
Cellular zinc ion homeostasis (GO 0006882)
Regulation of angiogenesis (GO 0045765)
Cellular response to cytokine stimulus (GO 0071345)
F
Substrate
Matrigel
Normal Peritoneum dECM
Neoplastic Peritoneum dECM
log2 normalized expression value
S100A8 MGP NNMT COMP TNR LOX COL1A2 DCN FBN2 VCAM1 SERPINE1 VWF EFEMP1 ASPN THBS2 EDIL3 DPT IGFBP7
Cell–Cell/Cell–Matrix interaction
Stiffness
Drug resistance

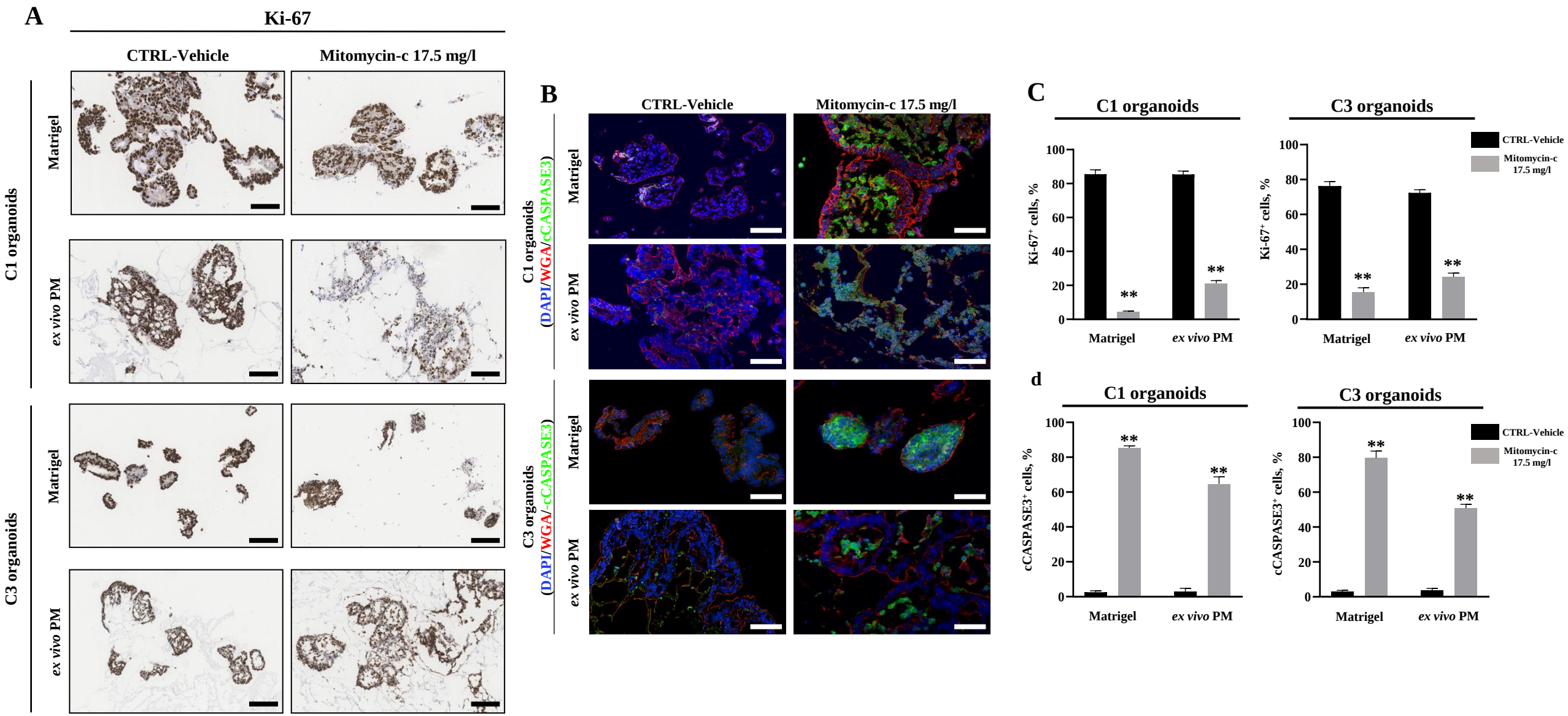
A
Ki-67
CTRL-Vehicle
Mitomycin-c 17.5 mg/l
C1 organoids
C3 organoids
Matrigel
ex vivo PM
B
CTRL-Vehicle
Mitomycin-c 17.5 mg/l
C1 organoids (DAPI/WGA/cCASPASE3)
C3 organoids (DAPI/WGA/-cCASPASE3)
Matrigel
ex vivo PM
C
C1 organoids
C3 organoids
Ki-67+ cells, %
CTRL-Vehicle
Mitomycin-c 17.5 mg/l
Matrigel
ex vivo PM
d
cCASPASE3+ cells, %
**

Figure 8